

Na-O Anticorrelation and HB. VII. The chemical composition of first and second-generation stars in 15 globular clusters from GIRAFFE spectra[★]

E. Carretta¹, A. Bragaglia¹, R.G. Gratton², S. Lucatello^{2,3}, G. Catanzaro⁴, F. Leone⁵, M. Bellazzini¹, R. Claudi², V. D'Orazi², Y. Momany^{2,6}, S. Ortolani⁷, E. Pancino¹, G. Piotto⁷, A. Recio-Blanco⁸, and E. Sabbi⁹

¹ INAF-Osservatorio Astronomico di Bologna, Via Ranzani 1, I-40127 Bologna, Italy

² INAF-Osservatorio Astronomico di Padova, Vicolo dell'Osservatorio 5, I-35122 Padova, Italy

³ Excellence Cluster Universe, Technische Universität München, Boltzmannstr. 2, D-85748, Garching, Germany

⁴ INAF-Osservatorio Astrofisico di Catania, Via S.Sofia 78, I-95123 Catania, Italy

⁵ Dipartimento di Fisica e Astronomia, Università di Catania, Via S.Sofia 78, I-95123 Catania, Italy

⁶ European Southern Observatory, Alonso de Cordova 3107, Vitacura, Santiago, Chile

⁷ Dipartimento di Astronomia, Università di Padova, Vicolo dell'Osservatorio 2, I-35122 Padova, Italy

⁸ Laboratoire Cassiopée UMR 6202, Université de Nice Sophia-Antipolis, CNRS, Observatoire de la Côte d'Azur, BP 4229, 06304 Nice Cedex 4, France

⁹ Space Telescope Science Institute, 3700 San Martin Drive, Baltimore, MD 21218, USA

Received 18 March 2009 / Accepted 31 May 2009

ABSTRACT

We present abundances of Fe, Na, and O for 1409 red giant stars in 15 galactic globular clusters (GCs), derived from the homogeneous analysis of high-resolution FLAMES/GIRAFFE spectra. Combining the present data with results from our FLAMES/UVES spectra and from previous studies within the project, we obtained a total sample of 1958 stars in 19 clusters, the largest and most homogeneous database of this kind to date. The programme clusters cover a range in metallicity from $[\text{Fe}/\text{H}] = -2.4$ dex to $[\text{Fe}/\text{H}] = -0.4$ dex, with a wide variety of global parameters (morphology of the horizontal branch, mass, concentration, etc.). For all clusters we find the Na-O anticorrelation, the classical signature of the operation of proton-capture reactions in H-burning at high temperature in a previous generation of more massive stars that are now extinct. Using quantitative criteria (from the morphology and extension of the Na-O anticorrelation), we can define three different components of the stellar population in GCs. We separate a primordial component (P) of first-generation stars, and two components of second-generation stars, that we name intermediate (I) and extreme (E) populations from their different chemical composition. The P component is present in all clusters, and its fraction is almost constant at about one third. The I component represents the bulk of the cluster population. On the other hand, E component is not present in all clusters, and it is more conspicuous in some (but not in all) of the most massive clusters. We discuss the fractions and spatial distributions of these components in our sample and in two additional clusters (M 3=NGC 5272 and M 13=NGC6205) with large sets of stars analysed in the literature. We also find that the slope of the anti-correlation (defined by the minimum O and maximum Na abundances) changes from cluster-to-cluster, a change that is represented well by a bilinear relation on cluster metallicity and luminosity. This second dependence suggests a correlation between average mass of polluters and cluster mass.

Key words. Stars: abundances – Stars: atmospheres – Stars: Population II – Galaxy: globular clusters – Galaxy: globular clusters: individual: NGC 104 (47 Tuc), NGC 288, NGC 1904 (M 79), NGC 2808, NGC 3201, NGC 4590 (M 68), NGC 5904 (M 5), NGC 6121 (M 4), NGC 6171 (M 107), NGC 6218 (M 12), NGC 6254 (M 10), NGC 6388, NGC 6397, NGC 6441, NGC 6752, NGC 6809 (M 55), NGC 6838 (M 71), NGC 7078 (M 15), NGC 7099 (M 30)

1. Introduction

At the turn of XXI century, the notion of GCs as true examples of simple stellar populations had to face a serious challenge. Astrophysicists realised that the long standing idea of

complete chemical homogeneity among stars within a cluster only applies to nuclei forged in core-collapse or thermonuclear supernovae (iron-group elements and the heaviest of the α -elements). On the other hand, lighter elements like C, N, O, Na, Mg, Al, and F (for which abundance measurements in GC stars were obtained only recently, e.g. Smith et al. 2005) show large star-to-star abundances variations. This pattern is clearly different from what observed among field stars in the same evo-

Send offprint requests to: E. Carretta, eugenio.carretta@oabo.inaf.it

[★] Based on observations collected at ESO telescopes under programmes 072.D-507 and 073.D-0211

lutionary stages, where only C and N (and Li) abundances are observed to change, while the abundances for the remaining light elements only reflect a typical pattern of supernova nucleosynthesis: field stars only populate a well-defined region at (constant at a given $[\text{Fe}/\text{H}]^1$) high O, low Na abundances.

Some years ago, the most popular explanation for the cluster stars peculiar compositions involved some degree of internal mixing due to the stars evolving along the red giant branch (RGB; see the review by Kraft 1994). However, it is currently well-established that, even if a certain degree of evolutionary mixing is present both in field (Gratton et al. 2000) and cluster (Smith and Martell 2003) stars, its impact is confined to Li, C, and N. The explanation for the observed star-to-star variations in the abundances of heavier nuclei, usually found to be anti-correlated (O and Na, Mg and Al), and even for the observed variations of CH and CN band strength in cluster turn-off stars (e.g. Cannon et al. 1998, Briley et al. 2004), had to be looked for elsewhere.

The key observation was the detection by Gratton et al. (2001) among unevolved stars in NGC 6752 and NGC 6397 of Na, O variations, anti-correlated with each other. This observation, confirmed afterward in other clusters (M 71=NGC 6838, Ramirez and Cohen 2002; 47 Tuc=NGC 104, Carretta et al. 2004a), definitively ruled out the possibility that the abundance variations are generated by processes occurring inside observed stars, because of the rather low central temperatures and thin convective envelopes of stars at the turn-off of GCs.

The scenario currently accepted invokes an external origin for the abundance variations, very likely the pollution from matter enriched with elements cycled through proton capture H-burning reactions at high temperature (Denisenkov & Denisenkova 1989, Langer et al. 1993) of the intra-cluster gas from which the stars, that we presently observe, did form out (see Gratton, Sneden and Carretta 2004 for a recent review).

This scenario requires that more than one stellar generation formed within each GC. It is very likely that this is the normal succession of events leading to the formation of these aggregates, since abundance variations are observed in each GC studied to date. However, the class of stars playing the role of major, early polluters cannot be established yet (e.g. fast rotating massive stars, Decressin et al. 2007; or intermediate-mass AGB stars, D’Antona and Ventura 2007 and references therein). What is clear is that the old definition of “abundance anomalies” can be dropped, and the more modern issue of the chemical composition and nature of second generation stars in GCs should be addressed.

This is the seventh paper in a series aimed at studying the mechanisms of formation and early evolution of stellar generations in GCs and, by investigating the relations between their properties and the global cluster parameters, the scenarios for the formation of the GCs themselves. The project is named *Na-O anticorrelation and horizontal branch (HB)*, its main emphasis being the possible link between the compositions of stars along the RGB and the HB morphology in GCs.

Such a connection has been suspected for a long time, with the He abundances as a *trait d’union*: He enhancement in cluster stars was invoked both by theoretical predictions of yields from rotating massive stars and intermediate mass asymptotic giant branch (AGB) stars and by photometric observations showing in some cases HBs with extremely long blue tails and multiple sequences (see the review by Cassisi et al. 2008 and Piotto 2009 for references and recent updates). The bottom line is that He-enhanced stars are likely to populate the blue extreme of the HBs and to also explain the extreme O-depletion observed in the surface abundances of RGB stars.

To better quantify the relation between the chemical composition of first/second generation stars and HB morphology, we started homogeneous analysis of the FLAMES spectra for more than 2000 stars in 19 GCs with different metallicity, HB morphology, and global parameters (mass, age, density, etc.).

The plan and the general strategy of our project has already been explained in the first paper of the series, so we briefly summarise it here for the convenience of the reader. Carretta et al. (2006a, hereafter Paper I) was dedicated to NGC 2808, the classical template for a bimodal distribution of HB stars. While explaining the tuning of the analysis procedures and tools for dealing with hundreds of stars in a large sample of GCs, previous papers were devoted to the study of particular objects. In Carretta et al (2007a, Paper II) we analysed NGC 6752, a cluster with a long blue HB and a relatively modest extension of the Na-O anticorrelation. Three papers (Gratton et al. 2006, 2007, and Carretta et al. 2007b, Paper III, V, and VI, respectively), focused on the two peculiar bulge clusters NGC 6441 and NGC 6388. Paper IV (Carretta et al. 2007c) dealt with the analysis of the Na-O anticorrelation in NGC 6218 and the first detection of a He-poor/He-rich stellar population among giant stars in GCs.

The collection and analysis of all the observational material is now complete and this unprecedented database of abundance ratios can be used to gain new insight into the formation processes leading to the GCs that we currently observe after nearly a Hubble time.

The aims of the present paper are three-fold: first, we present results from GIRAFFE spectra for the remaining 15 GCs in our sample, homogeneously deriving Fe, O, and Na abundances for about 1500 stars. Second, we combine the results from previous papers, to have the full set of observed Na-O anticorrelation in all 19 GCs from FLAMES/GIRAFFE. Third, data obtained from FLAMES/UVES spectra² will be merged with the GIRAFFE dataset to improve statistics and discuss on solid grounds the chemical composition of different stellar generations in GCs and to highlight their basic properties.

Inferences on cluster evolution and correlations with global cluster parameters derived from the present data will be thoroughly discussed in two forthcoming papers (Carretta et al. in preparation, Gratton et al. in preparation). The last two columns in Table 1 summarise for clarity the references to the papers

¹ We adopt the usual spectroscopic notation, *i.e.* $[X] = \log(X)_{\text{star}} - \log(X)_{\odot}$ for any abundance quantity X, and $\log \epsilon(X) = \log(N_X/N_H) + 12.0$ for absolute number density abundances.

² Except for NGC 6441 and NGC 6388, already published in Papers III and VI, the analysis of the UVES spectra is described in a companion paper, Carretta et al. (2009), hereinafter Paper VIII.

where the analysis of all GIRAFFE and UVES data is presented for each cluster in our project.

The paper is organised as follows: an outline of the target selection criteria and observations is given in Section 2, the derivation of atmospheric parameters and the analysis are described in Section 3, error estimates are briefly discussed in Sect. 4. In Section 5 we show the Na-O anticorrelation in all clusters and identify different components among the stellar populations in GCs, based on their chemical composition. The Na content of first and second-generation stars is discussed in Section 6. A dilution model for the Na-O anticorrelation is sketched in Section 7. Finally, a summary is presented in Section 8. In the Appendix a more detailed discussion of the procedure followed to estimate star-to-star and cluster errors is given.

2. Target selection and observations

Our foremost aim is to systematically and fully explore any possible connection between the chemical signature of different stellar populations in GCs and the distribution of stars in the colour-magnitude diagram (CMD) during the HB phase. We tried therefore to target GCs with the widest variety of HB morphologies.

We then selected clusters with a (stubby) red HB (NGC 104, NGC 6171, NGC 6838), with an HB populated from red to blue colours (NGC 3201, NGC 4590, NGC 5904, NGC 6121, NGC 7078) and with a predominantly blue HB (NGC 288, NGC 1904, NGC 6218, NGC 6254, NGC 6397, NGC 6752, NGC 6809, NGC 7099); some objects show a *very* extended blue HB (NGC 1904, NGC 6218, NGC 6254, NGC 6752, NGC 7078). Finally, three clusters with bimodal distributions in the HB (NGC 6388, NGC 6441, and NGC 2808, all also showing very extended blue HBs) were included among our targets.

In Table 1 some useful information are listed (Galactocentric radius, foreground reddening, apparent visual distance modulus, HB type, and metallicity $[\text{Fe}/\text{H}]$), taken from the updated online version of the catalogue by Harris (1996). In our sample we have clusters with metal abundances from $[\text{Fe}/\text{H}] = -2.4$ to about $[\text{Fe}/\text{H}] = -0.4$, spanning almost the whole metallicity range of the galactic GCs.

Figure 1 shows the location of our target GCs in a Sun-centred coordinate system³, superimposed on all clusters in the Harris’s (1996) database. Due to observational constraints, the clusters in our sample are, whenever possible, those lying nearer to the Sun’s location. However, apart from this obvious limitation, there is nothing peculiar in the spatial distribution of our sample (corresponding to about 13% of the ~ 150 known GCs in the Galaxy) with respect to the location of the other clusters.

The clusters can be grouped for age and kinematical properties according to the classical division introduced by Lee, Zinn

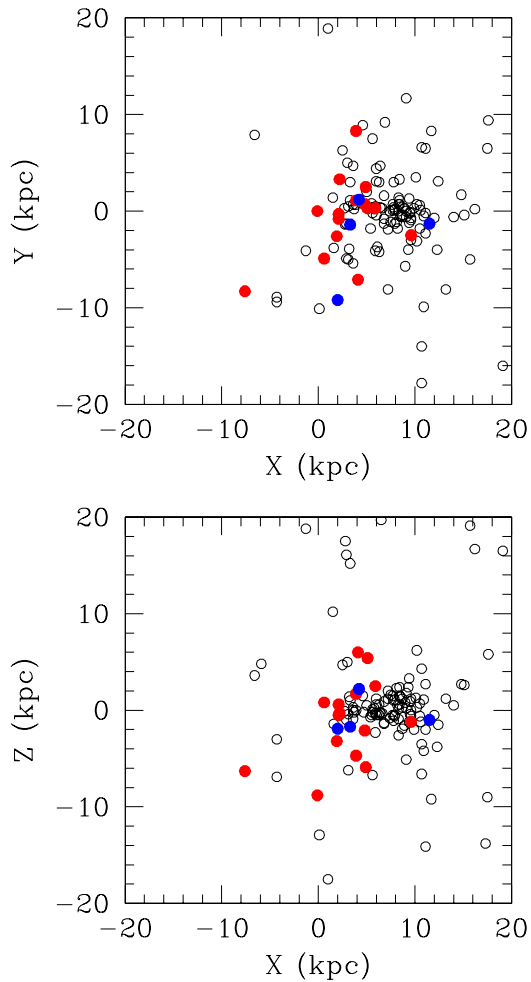


Fig. 1. Location of our target clusters in a Sun-centred coordinate system, where X points toward the Galactic centre, Y in the direction of Galactic rotation and Z toward the North Galactic Pole. Distance components are in kiloparsec. Filled red circles are GCs analysed in the present work and filled blue circles the GCs already published in this project, superimposed on all clusters in the Harris’s (1996) database.

and co-workers, whose latest and more complete compilation is from Mackey and van den Bergh (2005). We observed four so-called bulge/disc clusters (NGC 104, NGC 6388, NGC 6441, NGC 6838), 12 objects in the old halo group (NGC 288, NGC 1904, NGC 2808, NGC 5904, NGC 6121, NGC 6171, NGC 6218, NGC 6254, NGC 6397, NGC 6752, NGC 6809, NGC 7099) and three in the young halo subgroup (NGC 3201, NGC 4590, NGC 7078). Finally, the range in mass covers more than one order of magnitude, from $M_V = 71$ (NGC 6838, absolute magnitude $M_V = -5.60$ (Harris 1996) up to NGC 6441 ($M_V = -9.64$). It is noteworthy that five out of the nine most massive GCs in our Galaxy are in our sample. Summarizing, on the basis of Table 1 and Figure 1 we can be reasonably certain that our sample is representative of the global GC population, with no particular bias and/or selection effects.

The spectroscopic data were collected in service mode using the ESO high-resolution multifibre spectrograph

³ X points toward the Galactic centre, Y in the direction of Galactic rotation and Z toward the North Galactic Pole. Distance components are in kiloparsec.

FLAMES/GIRAFFE (Pasquini et al. 2002) mounted on the VLT UT2. Observations were done with two GIRAFFE setups, the high-resolution gratings HR11 (centred on 5728 Å) and HR13 (centred on 6273 Å), which were respectively chosen to measure the Na doublets at 5682-5688 Å and 6154-6160 Å and the [O I] forbidden lines at 6300, 6363 Å, as well as several lines of Fe-peak and α -elements. The spectral resolutions are $R=24,200$ (for HR11) and $R=22,500$ (for HR13), at the centre of the spectra. Total exposure times obtained for each cluster are listed in Table 1. The average seeing during the observations was less than 1.1 arcsec.

In Figure 2 we show a few examples of the spectra acquired with FLAMES/GIRAFFE and the HR11 and HR13 gratings in one metal-rich (47 Tuc=NGC 104), one metal-intermediate (M 5=NGC 5904), and one metal-poor cluster (M 30=NGC 7099). For each cluster we displayed stars in the middle and at the ends of the sampled range in temperature (magnitude), with typical S/N per pixel. As is evident also from this figure, the S/N is not a simple linear function of the magnitude, due to the different throughput of the fibres, and to slightly different degrees of precision in the centring of the targets in each fibre.

As done for the previous GCs (Papers I to VI), our targets were selected among isolated stars near the RGB ridge line⁴. To reduce concerns related to model atmospheres and ensure the sampling of sufficiently populated regions of the CMD, stars close to the RGB tip were generally avoided.

The number of actual cluster members observed in each cluster (as well as the typical S/N of the spectra) depends on several factors:

- a) the size of the cluster red giant population, which in turn depends mainly on the cluster mass and somewhat on the cluster distance (more massive/distant clusters allowed/forced us to observe brighter stars, less massive/more nearby clusters required/allowed us to shift down to fainter stars to gather enough targets to fully exploit the maximum number of dedicated fibres);
- b) the area covered by the cluster on the sky, which depends on its distance and concentration; for objects with smaller angular sizes we encountered more severe problems in positioning the FLAMES fibres (using the dedicated tool FPOSS). Hence, in the case of NGC 288 we observed stars at only 0.07 core radii from the cluster centre; in the opposite situation, for the highly concentrated and distant NGC 6388, the first sampled distance from the centre is about 17.5 core radii (but for every cluster all fibres were placed within its tidal radius);
- c) field stars contamination: this problem is exacerbated in particular for disc/bulge clusters such as NGC 6171, NGC 6388, NGC 6441, and NGC 6838. For these objects a somewhat limited number of member stars was observed. Moreover, we were forced to reject a number of potential target candidates in the most metal-poor clusters (e.g. NGC 7099, NGC 7078, NGC 4590) where the very small

number of (usually weak) lines hampered the assessment of the membership and the abundance analysis.

The approximate range in absolute V magnitude for stars observed in each cluster is given in Table 1. For several GCs this range extends down to luminosities fainter than the level of the RGB-bump.

We used the available optical photometry calibrated to the standard Johnson-Cousins system (Landolt 1992) for our target selection. The published photometric data are from Bellazzini et al. (2001) for NGC 288; Momany et al. (2003) for NGC 4590, NGC 7078, and NGC 7099⁵; Momany et al. (2004) for NGC 1904, and NGC 7099. Details on the other unpublished photometric catalogues are beyond the purpose of the present discussion, so we provide some brief information for reference. Clusters NGC 5904, NGC 6254, NGC 6397, and NGC 6809 were observed with the Wide Field Imager (WFI, FoV 33' \times 32'), mounted on the 2.2m ESO/MPI telescope in La Silla, Chile. For NGC 5904, B, V images were obtained with short (5 sec) and long (200-400 sec) exposures on UT 2000 July 7. The sky conditions were not optimal, with clouds and bad seeing, so the WFI photometry was only used to complement (in area) the B, V photometry by Sandquist et al. (1996), and was calibrated by comparison. For NGC 6254 the photometry is obtained from a couple of V and I images with exposure time 4 min and a couple of V and I images with 10 seconds. Instrumental magnitudes were obtained with Dophot (Schechter et al. 1993) and transformed into the standard Johnson/Kron-Cousins system using 84 secondary standard stars from the Stetson (2000) set that were in common with the cluster catalogue. Photometry for NGC 6397 and NGC 6809 consists in short (3-4 seconds and 5-8 seconds, respectively, for NGC 6397 and NGC 6809) and long (70-90 seconds and 90-180, respectively) V and B images (proposal 69.D-0582, P.I. Ortolani). For these two clusters, data were reduced using Daophot II (Stetson 1994) in IRAF⁶, and calibrated to the standard system. For NGC 3201 and NGC 6838, we adopted unpublished photometry kindly provided by C. Corsi and L. Pulone (private communication). For each cluster we used the Guide Star catalogue (GSC-2) to search for astrometric standards in the entire WFI image field of view. Several hundred astrometric GSC-2 reference stars were found in each chip, allowing us an accurate absolute position of the detected stars (~ 0.2 arcsec r.m.s. in both R.A. and Dec.). Finally, photometric and astrometric data for NGC 6388 are described in Paper VI.

A list of all the GIRAFFE target spectra retained in our final sample, together with coordinates, magnitudes, and radial velocities (RVs), is given in Table 2 (the full table is only available in electronic form at CDS). Together with the stars in the previously published clusters, and those with UVES spectra from Paper VIII, the number of objects with abundances

⁵ Data for NGC 104, NGC 6121, and NGC 6171 were not published, but were nevertheless reduced exactly like the others in Momany et al. (2003)

⁶ IRAF is distributed by the National Optical Astronomical Observatory, which are operated by the Association of Universities for Research in Astronomy, under contract with the National Science Foundation

⁴ All stars were chosen to be free from any companion closer than 2 arcsec and brighter than $V + 2$ mag, where V is the target magnitude.

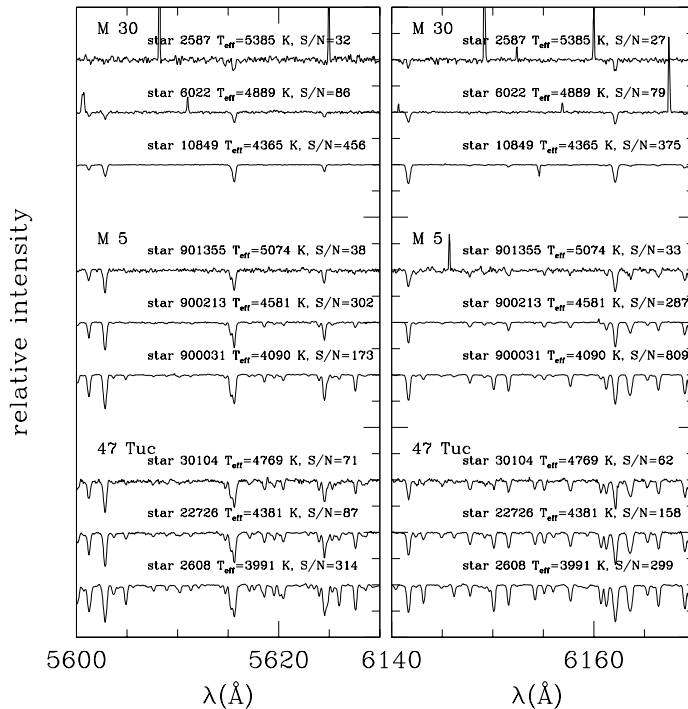


Fig. 2. Examples of observed spectra obtained with FLAMES/GIRAFFE and the HR11 (left panel) and HR13 (right panel) gratings. Displayed are portions of spectra of three stars in a metal-rich (47 Tuc=NGC 104), a metal-intermediate (M 5=NGC 5904), and a metal-poor cluster (M 30=NGC 7099). The stars are at the middle and at the extremes of the range in temperature (magnitude) sampled in each clusters. Spectra are normalised to the continuum and shifted by arbitrary quantities for display purposes. The effective temperatures and the S/N are indicated for each star.

derived from intermediate or high-resolution spectra is 1958. The project database increases by *an order of magnitude* the total number of RGB stars with abundance analysis in galactic GCs (the literature samples up to now consisted of a total of about 200 stars scattered among several clusters). Moreover, our abundance analysis is as homogeneous as currently possible, for the procedures for measuring equivalent widths (EW s), derivation of atmospheric parameters, list of atomic parameters, and set of model atmospheres.

Field stars (established on the basis of their radial velocities) were disregarded and excluded from further analysis if the measured RV differed by more than 3σ from the cluster average. In some cases, cross check of membership with available proper motions was possible (M4: Cudworth & Rees, 1990; M 5: Cudworth, 1979; NGC 6171: Cudworth et al. 1992; M 71: Cudworth 1985; M15: Cudworth 1976) and used to further clean out the member list. Contamination from stars on the AGB is only a minor source of concern for our analysis, because a priori the occurrence of AGB stars is expected to be at most about 10% of that of RGB stars. Moreover, the RGB and AGB are usually well separated at the luminosity of the observed stars. A posteriori, the very small scatter in derived iron abundances in each cluster ensures that we are using reliable atmospheric parameters, including the adopted stellar mass (appropriate for RGB).

We used the 1-D, wavelength-calibrated spectra as reduced by the dedicated Giraffe pipeline (BLDRS v0.5.3, written at the Geneva Observatory, see <http://girbldrs.sourceforge.net>). Radial velocities were measured using the IRAF package FXCORR with appropriate templates and are shown in Table 2.

Since we also aimed to target up to 14 stars per cluster with the dedicated UVES fibres (see Paper VIII), the GIRAFFE fibre positioning between the HR11 and HR13 pointings had to be changed. Because of this, not all the stars were observed with both gratings. Among a total of 1409 *bona fide* cluster members observed with GIRAFFE, 765 have spectra with both gratings, 320 only have HR11 observations, and 324 only HR13 observations. While we could recover Na abundances even for stars only observed with HR13 (at least for metal-rich clusters), since the weaker Na doublet at 6154-6160 Å falls into the spectral range covered by this setup, we could expect to measure oxygen for only a maximum of 1089 stars.

3. Atmospheric parameters and analysis

3.1. Atmospheric parameters

Temperatures and gravities were derived using the same procedure we described in the previous papers of the series (see Papers I to VI); along with the derived microturbulent velocities and iron abundances, they are listed in Table 3 (completely available only in electronic form at CDS) for all the 1409 stars

Table 1. Main characteristics of the target clusters and references.

GC		R_{GC}	E(B-V)	(m-M) _v	HBR	[Fe/H]	range M_V	Texp. (sec) HR11	Texp. (sec) HR13	Giraffe	UVES
NGC 104	47 Tuc	7.4	0.04	13.37	-0.99	-0.76	-1.1 ÷ +1.2	3200	1600	Paper VII	Paper VIII
NGC 288		12.0	0.03	14.83	0.98	-1.24	-1.7 ÷ +1.6	10800	5400	Paper VII	Paper VIII
NGC 1904	M 79	18.8	0.01	15.59	0.89	-1.57	-2.3 ÷ +1.5	11700	11700	Paper VII	Paper VIII
NGC 2808		11.1	0.22	15.59	-0.49	-1.15	-1.7 ÷ -0.1	8850	11700	Paper I	Paper VIII
NGC 3201		8.9	0.23	14.21	0.08	-1.58	-0.9 ÷ +2.5	3600	3600	Paper VII	Paper VIII
NGC 4590	M 68	10.1	0.05	15.19	0.17	-2.06	-0.8 ÷ +2.4	7200	10200	Paper VII	Paper VIII
NGC 5904	M 5	6.2	0.03	14.46	0.31	-1.27	-1.8 ÷ +1.6	4100	4100	Paper VII	Paper VIII
NGC 6121	M 4	5.9	0.36	12.83	-0.06	-1.20	-1.2 ÷ +1.2	950	950	Paper VII	Paper VIII
NGC 6171	M 107	3.3	0.33	15.06	-0.73	-1.04	+0.6 ÷ +2.4	8100	10800	Paper VII	Paper VIII
NGC 6218	M 12	4.5	0.19	14.02	0.97	-1.48	-2.0 ÷ +1.6	2700	2700	Paper IV	Paper VIII
NGC 6254	M 10	4.6	0.28	14.08	0.98	-1.52	-1.2 ÷ +1.8	2800	2800	Paper VII	Paper VIII
NGC 6388		3.2	0.37	16.14	-0.70	-0.60	-0.8 ÷ +1.6	31400	39100	Paper VII	Paper VI
NGC 6397		6.0	0.18	12.36	0.98	-1.95	-1.3 ÷ +2.4	900	900	Paper VII	Paper VIII
NGC 6441		3.9	0.47	16.79	-0.70	-0.53	-0.6 ÷ +0.3	10600	10600	Paper V	Paper III
NGC 6752		5.2	0.04	13.13	1.00	-1.56	-1.3 ÷ +1.4	1750	1750	Paper II	Paper VIII
NGC 6809	M 55	3.9	0.08	13.87	0.87	-1.81	-2.5 ÷ +1.5	4100	2200	Paper VII	Paper VIII
NGC 6838	M 71	6.7	0.25	13.79	-1.00	-0.73	-0.2 ÷ +1.2	2700	2700	Paper VII	Paper VIII
NGC 7078	M 15	10.4	0.10	15.37	0.67	-2.26	-2.6 ÷ +1.6	8100	8100	Paper VII	Paper VIII
NGC 7099	M 30	7.1	0.03	14.62	0.89	-2.12	-2.0 ÷ +2.6	5400	5400	Paper VII	Paper VIII

Galactocentric distance, coordinates, foreground reddening, apparent visual distance modulus, horizontal branch ratio $HBR=(B-R)/(B+V+R)$, and metallicity from the catalogue by Harris (1996) and web updates.

Table 2. List and relevant information for the 1409 target stars. The complete table is available electronically only at CDS.

GC	ID	RA	Dec	B	V	I	K	RV(HR11)	RV(HR13)	Notes
NGC 104	1389	0 24 7.423	-71 56 56.67	14.855	13.847	0.000	11.099		-16.63	HR13
NGC 104	2608	0 25 0.617	-71 55 58.66	13.654	12.250	0.000	8.617	-26.73	-26.97	HR11,HR13
NGC 104	2871	0 24 40.034	-71 55 45.03	14.950	13.983	0.000	11.321	-20.73		HR11
NGC 104	4373	0 23 18.186	-72 11 51.64	15.292	14.345	0.000	11.978	-10.94	-11.51	HR11,HR13
NGC 104	5172	0 23 9.787	-72 11 18.38	14.861	13.823	0.000	11.292	-18.01	-18.48	HR11,HR13

Table 3. Adopted atmospheric parameters and derived iron abundances. The complete Table is available electronically only at CDS.

GC	Star	T_{eff} (K)	$\log g$ (dex)	[A/H] (dex)	v_t (km s ⁻¹)	nr	[Fe/H] _r (dex)	rms	nr	[Fe/H] _{ii} (dex)	rms
NGC 104	1389	4568	2.09	-0.78	1.66	21	-0.775	0.131	2	-0.724	0.208
NGC 104	2608	3991	0.99	-0.77	1.64	44	-0.770	0.159	3	-0.748	0.084
NGC 104	2871	4609	2.17	-0.74	1.10	19	-0.737	0.106			
NGC 104	4373	4709	2.38	-0.80	1.42	44	-0.800	0.198	4	-0.732	0.170
NGC 104	5172	4560	2.08	-0.71	1.35	40	-0.711	0.137	3	-0.753	0.029

having GIRAFFE spectra in the 15 clusters analysed in this work.

Effective temperatures (T_{eff}) were obtained in two steps. We derived first estimates of T_{eff} and bolometric corrections (B.C.) for our stars from $V - K$ colours, where V is from our photometry and K was taken from the Point Source Catalogue of 2MASS (Skrutskie et al. 2006) and transformed to the TCS photometric system, as used in Alonso et al. (1999). We employed the relations by Alonso et al. (1999, with the erratum of 2001). For all clusters the distance moduli, values of foreground reddening, input metallicities as listed in Table 1 (Harris 1996) were adopted, and the relations $E(V - K) = 2.75E(B - V)$, $A_V = 3.1E(B - V)$, and $A_K = 0.353E(B - V)$

(Cardelli et al. 1989). We checked that the use of more recent relations between monochromatic absorption and reddening, like those of Fitzpatrick (1999), including dependence of reddening corrections on stellar colours, has negligible impact in our analysis, with differences in the temperatures < 10 K.

In the second step, as in Paper II and the subsequent papers of this project, the final adopted T_{eff} were derived from a relation between T_{eff} (from $V - K$ and the Alonso et al. calibration) and V or K magnitude. To derive this relation, we used “well-behaved” stars in each cluster (i.e. stars with magnitudes in both visual and infrared filters and lying on the RGB). This procedure was adopted to decrease the scatter in abundances due to uncertainties in temperatures, since magnitudes

are much more reliably measured than colours. The assumptions behind this approach are discussed in Paper II to which we refer the reader for details.

Surface gravities $\log g$ were obtained from the apparent magnitudes, the above effective temperatures and distance moduli, and the bolometric corrections from Alonso et al. (1999), assuming masses of $0.85 M_{\odot}$ ⁷ and $M_{\text{bol},\odot} = 4.75$ as the bolometric magnitude for the Sun. As usual, we derived values of the microturbulent velocities v_t 's by eliminating trends in the relation between abundances from Fe neutral lines and expected line strength (see Magain 1984).

Final metallicities were then obtained by interpolating, in the Kurucz (1993) grid of model atmospheres (with the option for overshooting on), the model with the proper atmospheric parameters whose abundance matches that derived from Fe I lines.

3.2. Equivalent widths and iron abundances

Adopted line lists, atomic parameters, and reference solar abundances (from Gratton et al. 2003) are strictly homogeneous for all stars analysed in the present programme. Equivalent widths (*EWs*) were measured as described in detail in Bragaglia et al. (2001) with the same automatic procedure we used in the previous analysis of GIRAFFE spectra (Papers I, II, VI, V) for the definition of the local continuum around each line. This is a crucial step at the limited resolution of our spectra, especially for the coolest targets.

As in the previous papers, we corrected the *EWs* measured in the intermediate-resolution GIRAFFE spectra to the system defined by the high-resolution UVES spectra, using the stars observed with both instruments in each cluster (see Paper VIII). This correction was deemed necessary since the contribution of unrecognised blends can cause an overestimate of the *EWs* measured on intermediate resolution spectra. On the other hand, veiling from very weak lines, again not recognizable on lower resolution spectra, might lower the true continuum, resulting into an underestimate of measured *EWs*.

In 13 out of 15 clusters we had a number of stars observed with both instruments, from a minimum of five up to 13 stars, with an average of about 10 stars per cluster. However, in NGC 1904 and NGC 6838, no stars in common between the UVES and GIRAFFE samples were available. In the first case we used five UVES stars with a *relative difference* in effective temperature within 10 K from five GIRAFFE stars for our comparison: since the cluster does not show any large intrinsic scatter in element ratios (obviously, with the exceptions of Na, O, Mg, and Al lines), this is a reasonable approach. In the case of NGC 6838, the target stars of UVES observations are much cooler than those observed with GIRAFFE and a similar comparison is impossible. To correct the *EWs* in this cluster we then applied the average relation derived from the other 13 GCs. Figure 3 shows the comparison between the *EWs* measured on UVES spectra and the corrected *EWs* from GIRAFFE spectra. After this correction the average dif-

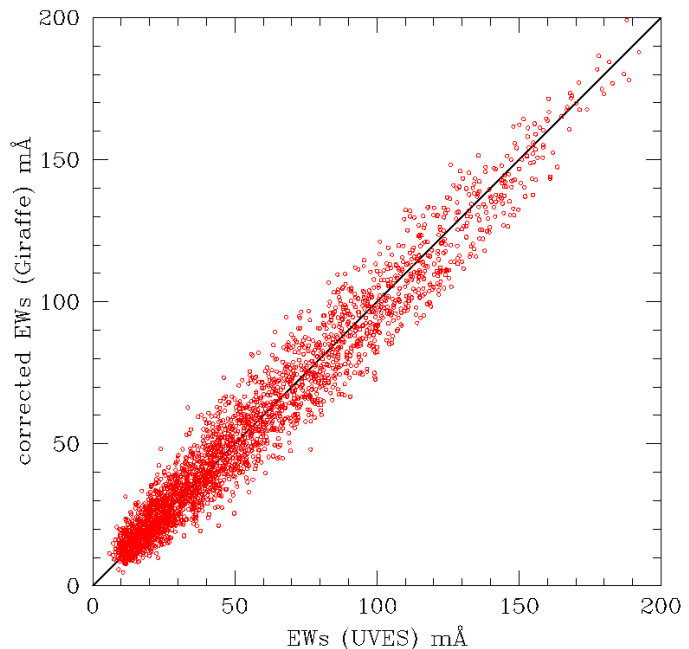


Fig. 3. Comparison between the *EWs* measured on high-resolution FLAMES/UVES spectra and those measured for the same stars on the GIRAFFE spectra, after they were corrected to the system of the UVES *EWs* (see text).

ference (in the sense UVES minus GIRAFFE) is $+0.1 \pm 0.2 \text{ mÅ}$ ($rms = 8.1 \text{ mÅ}$) from 2811 lines.

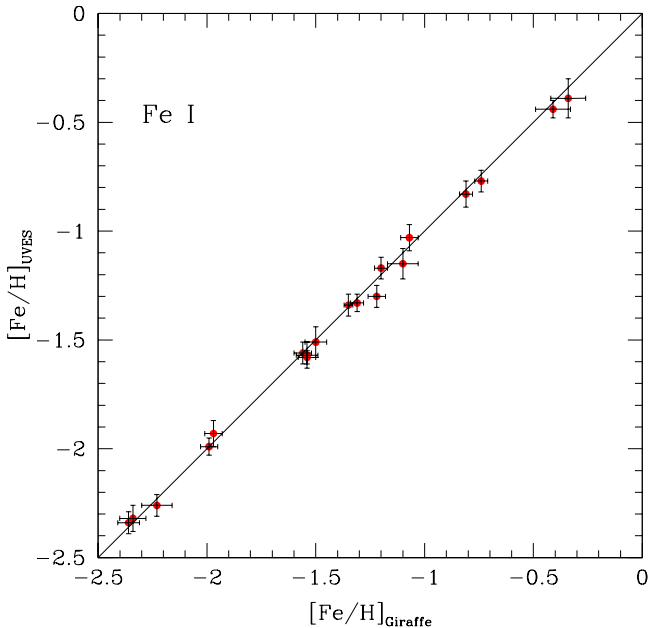
Average abundances of iron for the 15 programme clusters derived from our GIRAFFE spectra, are listed in Table 4. As a comparison, average metallicities derived from the analysis of UVES spectra (Paper VIII) are reported in the second column of this table. The agreement is very good, with the average difference $0.007 \pm 0.008 \text{ dex}$ with $rms = 0.033 \text{ dex}$. We are practically on the same scale, as also demonstrated in Figure 4, where we included the four clusters previously analysed in this series. This check is relevant, since in the following we merge results for [O/Fe] and [Na/Fe] ratios obtained from the samples of stars observed with both UVES and GIRAFFE.

Metal abundances ([Fe/H]) obtained from the analysis of GIRAFFE spectra are listed in the form $[\text{Fe}/\text{H}] \pm \text{err1} \pm \text{err2}$ dex, where the first error refers to the statistical errors and the second one is relative to the cluster or systematic error (see Appendix A). The *rms* scatter and the number of stars used in the averages are given in columns 5 and 6 of Table 4. The last 3 columns concern the abundances of iron derived from the singly ionised species; generally, the two averages agree very well, although the *rms* scatter associated to the $[\text{Fe}/\text{H}]_{\text{II}}$ abundance ratio is higher. We point out that the number of useful Fe II lines in the spectral range covered by HR11 and HR13 is very limited, at most 1 or 2. Moreover, we remind the reader that one of the criteria in the star selection was to choose stars as far away as possible from the tip of RGB to avoid concerns related to continuum placement and remain in the temperature regime where model atmospheres are more reliable. Hence, lines of Fe II are not strong for these rather warm, high-

⁷ We note that the derived values of surface gravity are not very sensitive to the exact value of the adopted mass

Table 4. Average iron abundances from UVES (from Paper VIII) and GIRAFFE spectra.

GC	[Fe/H] UVES (dex)	[Fe/H]I±stat.err. GIRAFFE (dex)	syst. error (dex)	<i>rms</i> (dex)	N. stars	[Fe/H]II (dex)	<i>rms</i> (dex)	N.stars
NGC 104	-0.768	-0.743±0.003	±0.026	0.032	147	-0.769	0.075	110
NGC 288	-1.305	-1.219±0.004	±0.070	0.042	110	-1.231	0.092	72
NGC 1904	-1.579	-1.544±0.005	±0.069	0.036	58	-1.483	0.061	50
NGC 3201	-1.512	-1.495±0.004	±0.073	0.049	149	-1.403	0.106	99
NGC 4590	-2.265	-2.227±0.006	±0.068	0.071	122	-2.233	0.108	10
NGC 5904	-1.340	-1.346±0.002	±0.062	0.023	136	-1.348	0.072	109
NGC 6121	-1.168	-1.200±0.002	±0.053	0.025	103	-1.197	0.056	80
NGC 6171	-1.033	-1.065±0.008	±0.026	0.044	33	-1.053	0.085	26
NGC 6254	-1.575	-1.556±0.004	±0.074	0.053	147	-1.558	0.091	102
NGC 6388	-0.441	-0.406±0.013	±0.028	0.078	36	-0.351	0.158	29
NGC 6397	-1.988	-1.993±0.003	±0.060	0.039	144	-1.985	0.077	32
NGC 6809	-1.934	-1.967±0.004	±0.072	0.044	156	-1.933	0.060	111
NGC 6838	-0.832	-0.808±0.005	±0.048	0.034	39	-0.801	0.065	39
NGC 7078	-2.320	-2.341±0.007	±0.067	0.061	84	-2.352	0.091	27
NGC 7099	-2.344	-2.359±0.006	±0.067	0.046	64	-2.289	0.085	14

**Fig. 4.** Metal abundances obtained from GIRAFFE spectra compared with [Fe/H] I ratios derived from high-resolution UVES spectra for programme GCs. In this plot we also included the 4 clusters (NGC 2808, NGC 6752, NGC 6218, and NGC 6441) already analysed in previous papers. Error bars are 1σ *rms* scatter.

gravity stars, and the effect is exacerbated for clusters at very low metallicity.

The agreement we found is a good sanity check, since the ionisation equilibrium for Fe is quite sensitive to any possible problem in the abundance analysis, whereas the differences we obtained are almost negligible.

Other diagnostic diagrams are shown in Figure 5. In the upper panel, the final slope in the relation of the expected line

strength vs Fe I abundances for each of the 1409 individual stars with GIRAFFE spectra in the 15 clusters is plotted as a function of temperature, coded according to the gratings. Apart from very few stars (mainly some warm and metal-poor stars observed with HR11 only where there are just a few Fe I lines⁸), most slopes are near zero: the average value is 0.000 ± 0.000 *rms* = 0.004 (1293 stars), after a 2.5σ -clipping to exclude outliers.

Panel (b) in Figure 5 displays the slopes of the relation between abundances from neutral Fe I lines and excitation potential for each analysed star, as a function of the effective temperature adopted. After 126 outliers in the plot are eliminated in a 2.5σ -clipping, the average value for this slope turns out to be -0.023 ± 0.001 with *rms* = 0.043 (1403 stars). In turn, this implies that on average the temperatures we derive from colours are higher than those we would derive from the excitation equilibrium by about 80 K.

If we plot this slope as a function of the metallicity of individual stars, we see that the difference increases with decreasing metallicity. A possible explanation is that at low metallicities we are seeing a more marked influence of departures from the LTE assumption, and/or an atmospheric structure not reproduced well by one-dimensional model atmospheres, as suggested by Asplund et al. (1999). Both effects are likely to be more relevant in low metallicity stars, where the atmosphere is more transparent.

In the panel (c) we show the difference for each star between the individual [Fe/H] I value and the average value for the cluster, in order to plot in the same plane all stars in GCs of different metallicities. These differences run flat across a temperature range of about 1600 K, the average difference being -0.001 ± 0.001 , *rms* = 0.041 dex (1480 stars, again after a 2.5σ -clipping). Finally, the lower panel in Figure 5 illustrates the good agreement between iron abundances from Fe I and

⁸ In these cases we chose not to force the zeroing of the relation Fe I abundances vs line strength, due to the associated large uncertainties in the resulting fit because of the very few lines available.

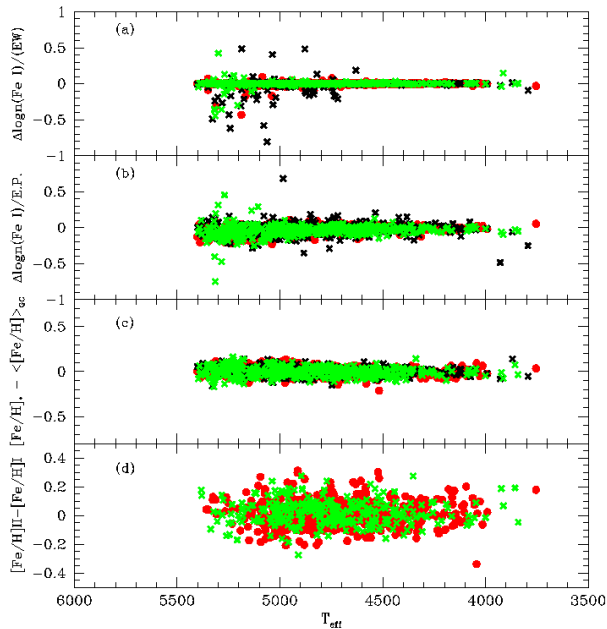


Fig. 5. Diagnostic diagrams for the analysis of 1409 stars with GIRAFFE spectra in the 15 GCs analysed here. (a): slope of the relation between expected line strength and Fe I abundances used to derive the ν_i values for each individual stars. (b) slope of the relation between Fe I abundances and excitation potential E.P. for each star. (c): the average $[\text{Fe}/\text{H}]$ value for each cluster is subtracted from the metallicity of each star in the cluster, and the differences are shown. (d): differences in iron abundances from Fe I and Fe II lines. All quantities are plotted as a function of the effective temperature. Filled red circles indicate stars with observations in both HR11 and HR13 gratings; green and black crosses, are for stars observed only with HR13 and HR11, respectively.

Fe II species over the whole range in temperature and cluster metallicities (after culling out 34 outliers, the average value is $+0.016 \pm 0.002$, $rms = 0.072$ dex, from 868 stars.)

4. Errors in the atmospheric parameters and cosmic spread in iron

The error estimate in abundance analysis is often a poorly explained issue. In most cases there is a certain degree of confusion between internal errors, systematic errors and sensitivities of abundances to changes in the atmospheric parameters. In some cases, only the last quantities are given in the papers, with no actual estimate of errors on the derived abundances.

The procedure for error estimates perfected in previous papers of this series is purposely tailored to deal with the approach we used to obtain the atmospheric parameters required for the analysis. In particular, we emphasise the two steps followed: first, we derived first-guess temperatures from $V-K$ colours, less sensitive to the metal abundances than other colour indices. Second, we then derived the final adopted T_{eff} 's from a relation between temperature on the Alonso et al. scale

and magnitude, under the assumptions (verified in each case) that the stars involved all belong to the RGB and that there is no intrinsic spread in abundances in the cluster. This second step (when using the infrared K magnitudes from 2MASS) greatly alleviates problems in clusters with high and likely differential values of the reddening, as demonstrated by the small rms scatters we obtain in the iron distributions even in GCs (e.g. NGC 6388, NGC 6254) well known for being affected by this phenomenon. Moreover, using this relation results in a sharp decrease in the star-to-star errors, since magnitudes are more easily measured than colours, in particular for our rather bright programme stars.

A detailed description of the whole error estimate can be found e.g. in Paper IV and will not be repeated here, as it is beyond the aim of the present discussion. The interested reader may find an extensive discussion in the appendix of the present paper, with tables of sensitivities, estimates of the actual errors in the atmospheric parameters, and resulting uncertainties in abundances. In Appendix A we clearly separate the individual, star-to-star errors (relevant to the discussion of the abundance spread in each cluster) from the cluster errors, which concern the whole cluster sample.

The expected star-to-star scatter in $[\text{Fe}/\text{H}]$ caused by the three major (T_{eff} , ν_i , EW) or to all error sources (last two columns in Table A3 in the Appendix) may be compared to the *observed* scatter (defined as the rms scatter of all stars in each cluster, column 5 in Table 4). We note that, for at least half of our sample, the expected scatter is formally higher than the observed spread, even taking the statistical uncertainty into account. This may be due to an overestimate of some error sources or to correlations and it does not invalidate the conclusion that globular clusters are very homogeneous (concerning Fe content) objects. Most of our programme clusters are homogeneous in $[\text{Fe}/\text{H}]$ at a level below 10%, and when higher quality data are available (as in NGC 5904, NGC 6121) the level that any theoretical model of cluster formation has to reproduce drops to a 6% degree of homogeneity involving products from supernovae nucleosynthesis. We stress that this is a very strong constraint to be satisfied.

Finally, typical star-to-star errors are 0.14 dex in $[\text{O}/\text{Fe}]$ and 0.08 dex in $[\text{Na}/\text{Fe}]$, on average (see Appendix A, Table A2).

5. Results and discussion

5.1. The Na-O anticorrelation

We derived abundances of O and Na from measured EW 's. In principle, among the 1409 member stars observed with FLAMES/GIRAFFE and with atmospheric parameters and Fe determination in our 15 clusters we could expect to measure O in a maximum of 1089 stars, all those observed with the HR13 grating.

However, although all oxygen lines were carefully inspected by eye, the combination of unfavourable observational constraints (too low a S/N , the faintness of stars in not well-populated clusters) and/or of physical ingredients (very large O-depletions, cluster low metallicity) prevented the O abun-

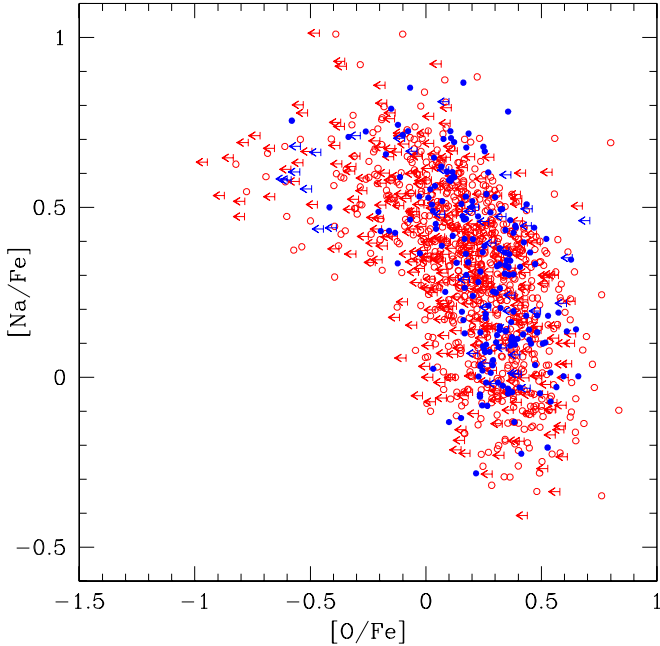


Fig. 6. The Na-O anticorrelation for a grand total of 1958 individual red giant stars in the 19 GCs of our project. $[\text{Na}/\text{Fe}]$ and $[\text{O}/\text{Fe}]$ ratios from GIRAFFE spectra are shown as open (red) circles; abundance ratios obtained from UVES spectra (Paper VIII) are superimposed as filled (blue) circles and show no offset from the GIRAFFE sample. Arrows indicate upper limits in oxygen abundances.

dance to be derived in all stars. We measured O abundances in a subsample of 865 stars, including 313 upper limits.

Oxygen abundances were obtained from the forbidden $[\text{O} \text{ I}]$ lines at 6300.3 and 6363.8 Å; the former was cleaned from telluric contamination by H_2O and O_2 lines using a synthetic spectrum, as described in Paper I. Our experience with the analysis of the first four clusters is that the contribution of the high excitation Ni I line at 6300.34 Å to the measured EW is negligible (see also Paper II), and the CO formation does not have a relevant impact on the derived O abundances due to the rather high temperature of our programme stars.

Sodium abundances could be obtained for many more stars, since at least one of the Na I doublets at 5672-88 Å and at 6154-60 Å is always available (depending on the GIRAFFE setup used). Again, the Na measurements were interactively checked by eye in all cases where clear discrepancies between abundances from the 2 to 4 different lines were present. Derived average Na abundances were corrected for effects of departures from the LTE assumption according to the prescriptions by Gratton et al. (1999).

This was our first step and it produced the number of stars with both O and Na abundances derived from GIRAFFE spectra listed in column 2 of Table 5, where for completeness we included also the number of stars used in the Na-O anticorrelation in the four previously analysed clusters.

Afterward, we checked for possible systematic effects in Na abundances as derived from the two doublets. On average,

there are no large systematic differences, the mean difference in the sense 6154-60 Å minus 5682-88 Å being $\Delta \log n(\text{Na}) = +0.001 \pm 0.007$ dex, with $rms = 0.181$ dex from 678 stars.

However, we studied a large sample of stars in clusters spanning almost 2 dex in metallicity, and we detected a subtle statistical bias by plotting the differences as a function of $[\text{Fe}/\text{H}]$. When the Na I lines at 6154-60 Å are very weak, they are measurable only when spuriously enhanced by noise. This suggests that we can overestimate the Na abundance using these lines in particular in metal-poor and warmer stars. To correct for this effect we used an empirical parameter, defined as $(T_{\text{eff}}/100) - 10 \times [\text{Fe}/\text{H}]$.

If this parameter was larger than 65, then

- if only lines belonging to the 6154-60 Å doublet were available for the star, they were eliminated and the star was thus dropped from the Na-O anticorrelation;
- for stars with 2, 3, 4 lines of Na, average $[\text{Na}/\text{Fe}] > 0.2$ dex and $rms(\text{Na}) < 0.2$ dex, all the lines were retained;
- for stars with 2, 3, 4 lines of Na and $rms(\text{Na}) > 0.2$ dex, the 6154-60 Å lines were deleted;

After this correction (culling out stars, in particular in the most metal-poor clusters), the number of stars participating to the Na-O anticorrelation is the one listed in column 3 of Table 5.

Finally, our third step was to combine chemical composition measurements derived from the GIRAFFE spectra sample with Na and O abundances derived from the analysis of UVES spectra, for which analysis and element ratios are discussed in Paper VIII. Regarding Fe, Na, and O, it suffices to say here that we followed the same procedures used for the GIRAFFE spectra, both to obtain atmospheric parameters and the abundance ratios.

There are 214 stars with UVES spectra analysed in the 19 clusters of our complete sample; of these, 172 stars are in the 15 clusters of the present work, 170 of which have both O and Na. $[\text{Na}/\text{Fe}]$ and $[\text{O}/\text{Fe}]$ abundance ratios from UVES spectra are superimposed to the same ratios from GIRAFFE spectra in Figure 6. This figure shows that there is no obvious offset between the two data sets and, together with the very good agreement obtained in iron abundances (see Figure 4), this guarantees that the two samples can be safely merged without introducing any bias.

This is a crucial point for some clusters, especially for NGC 6397, where only a handful of O detections (mostly upper limits) could be extracted from the GIRAFFE spectra. Hence, the final step in exploring the Na-O anticorrelation in our programme clusters was to substitute O and Na values obtained from the UVES spectra for stars observed with both instruments and to add the values from stars with only UVES observations.

In Table 6 we list the abundances of O and Na (the complete table is available only in electronic form at CDS) in each star of the present subsample of 15 GCs. For O we distinguish between actual detections and upper limits. The number of measured lines and the rms values are also indicated.

Column 4 of Table 5 provides the final numbers of stars that we used to build the Na-O anticorrelation in each of the 19

Table 5. Number of stars with both Na and O and fraction of the primordial, intermediate, and extreme components

GC	N.stars	N.stars	N.stars	fraction	fraction	fraction
	(O,Na)	(O,Na)	(O,Na)	P	I	E
	GIRAFFE	GIR.+corr	GIR.+UVES	component	component	component
NGC 104	109	109	115	27 ± 5	69 ± 8	4 ± 2
NGC 288	64	64	70	33 ± 7	61 ± 9	6 ± 3
NGC 1904	49	39	48	40 ± 9	50 ± 10	10 ± 5
NGC 2808	91	91	98	50 ± 7	32 ± 6	18 ± 4
NGC 3201	104	94	100	35 ± 6	56 ± 7	9 ± 3
NGC 4590	48	36	44	40 ± 9	60 ± 11	0 ^{+4.1} _{-0.0}
NGC 5272			37	32 ± 9	68 ± 14	0 ^{+4.6} _{-0.0}
NGC 5904	106	106	114	27 ± 5	66 ± 8	7 ± 2
NGC 6121	80	80	88	30 ± 6	70 ± 9	0 ^{+2.1} _{-0.0}
NGC 6171	27	27	30	33 ± 11	60 ± 14	7 ± 5
NGC 6205			53	34 ± 8	45 ± 9	21 ± 6
NGC 6218	67	67	74	24 ± 6	73 ± 10	3 ± 2
NGC 6254	99	77	87	38 ± 7	60 ± 8	2 ± 2
NGC 6388	29	29	32	41 ± 11	41 ± 11	19 ± 8
NGC 6397	6	3	16	25 ± 13	75 ± 22	0 ^{+12.0} _{-0.0}
NGC 6441	24	24	29	38 ± 11	48 ± 13	14 ± 7
NGC 6752	89	89	98	27 ± 5	71 ± 9	2 ± 1
NGC 6809	105	75	84	20 ± 5	77 ± 10	2 ± 2
NGC 6838	31	31	42	29 ± 8	71 ± 13	0 ^{+4.2} _{-0.0}
NGC 7078	37	20	33	39 ± 11	61 ± 14	0 ^{+5.5} _{-0.0}
NGC 7099	27	19	29	41 ± 12	55 ± 14	3 ± 3

clusters of this project. We have a grand total of 1235 red giants with O and Na abundances derived homogeneously (936 in the 15 clusters analysed here), by far *the largest sample collected up to date*.

In Figure 7 the Na-O anticorrelation we obtain in all the 19 clusters is shown, with star-to-star error bars plotted in each panel. In these plots we used all available stars in each cluster with both Na and O abundances, irrespective of their derivation from GIRAFFE or UVES (Paper VIII) spectra.

We also searched the literature for GCs not included in our programmes, with a large ($> 30 - 40$) number of stars analysed, and with O and Na abundances from high-resolution spectra. We only found two GCs meeting these requirements: NGC 5272 (M 3) and NGC 6205 (M 13). For these clusters we used the stars analysed in the most recent studies (Snedden et al. 2004 and Cohen and Melendez 2005), corrected to our scale of solar reference abundances, and merged their samples with ours, adopting for stars in common those from Sneden et al. The final adopted numbers of stars are reported in column 4 of Table 5.

For several clusters in our sample, this is the first-ever survey of this kind based on a very large numbers of stars. For example, since it is a nearby and luminous cluster, 47 Tuc is often used as a yardstick for abundance analysis, but only a few stars were previously observed and analysed. To our knowledge, our homogeneous database of 115 red giants in this cluster is the largest collected to extensively study the Na-O signature in this object. Within the present project, the Na-O anticorrelation is traced and also studied for the first time for several other clusters: NGC 1904, NGC 2808 (apart from 19 stars from Carretta et al. 2004b), NGC 4590, NGC 6171, NGC 6397, NGC 6441, NGC 6809, and NGC 7099. The wide range in HB morphol-

ogy, metallicity and other cluster parameters strengthens the suggestion (see Carretta 2006) that this signature is present in *all* clusters where data allows us to investigate it, and it is probably related to the same mechanism of formation and early evolution of GCs.

In some cases the number of stars available to probe the Na-O anticorrelation is limited by the number of stars that turned out to be actual cluster members. This was the case for the disc clusters NGC 6171 and NGC 6838 and for the bulge clusters NGC 6441 (Paper V) and NGC 6388. In very metal-poor clusters the number of stars in the [Na/Fe]–[O/Fe] plane is lower than expected because of the difficult task of measuring in particular the forbidden [O I] lines, the worst case being NGC 6397 where only the addition of measurements from UVES spectra allows us to derive the observed anticorrelation.

The distribution function of the [O/Na] ratios from our data (including both GIRAFFE and UVES observations) is shown in Figure 8 for all the 15 clusters analysed here plus the four clusters already studied. In each panel, the histograms are normalised to the total number of stars with O and Na abundances.

5.2. The primordial, intermediate, and extreme components

The presence of large star-to-star variations in abundance of elements that cannot be produced in presently observed low-mass red giants is the clearcut proof of the existence in GCs of at least two different stellar generations.

The ratio of the number of first to second-generation stars could be very useful for constraining any formation scenario (see e.g., D’Ercole et al. 2008). However, to truly be meaningful, such a quantity must be derived from large samples of stars

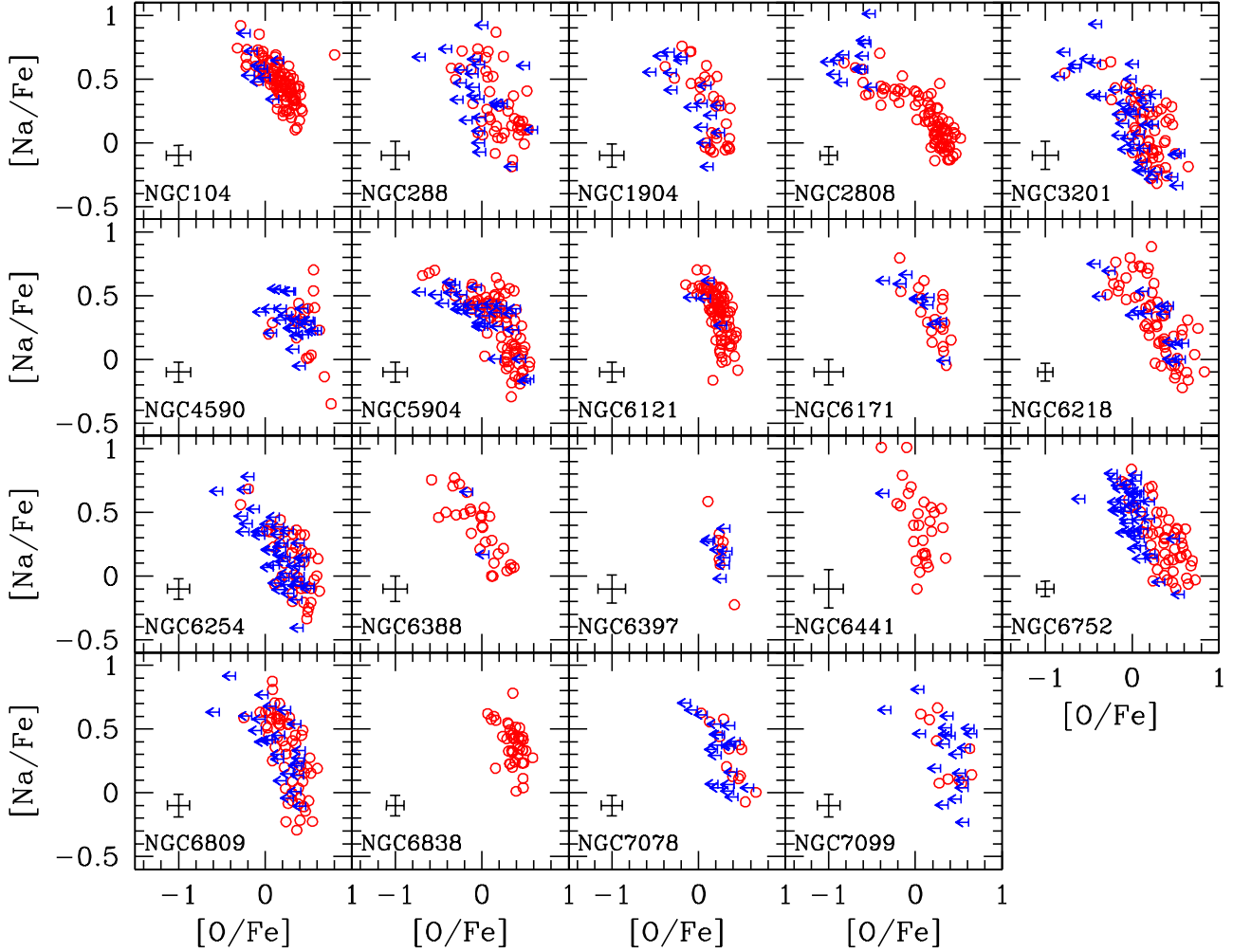


Fig. 7. The Na-O anticorrelation observed in all the 19 GCs of our project. All stars with Na and O abundances from GIRAFFE and UVES (Paper VIII) spectra are used. Star-to-star error bars (see Appendix A) are indicated in each panel. Upper limits in O abundances are shown as arrows, detections are indicated as open circles.

Table 6. Abundances of O and Na for the 1409 stars with only GIRAFFE spectra in 15 GCs. The complete Table is available only in electronic form at CDS.

GC	Star	nr	[O/Fe]	rms	nr	[Na/Fe]	rms	HR	lim
NGC 104	1389	2	0.395	0.069	2	+0.175	0.011	1	1
NGC 104	2608	1	-0.207		4	+0.615	0.078	2	1
NGC 104	2871				2	+0.440	0.062	3	1
NGC 104	4373	1	0.430		4	+0.249	0.135	2	1
NGC 104	5172	2	0.189	0.002	4	+0.489	0.072	2	1

all analysed in the same way, to avoid introducing spurious effects reflecting possible offsets in the analyses.

Our database offers the unique, unprecedented opportunity to study the behaviour of about 1,600 red giants in a significant fraction of the whole galactic GC population. We sampled red giant stars with no obvious bias with respect to their Na and O abundances. We could not measure O abundances in all stars, and we only placed upper limits to O abundances in many stars, generally warm, metal-poor, and O-poor. In spite of this

limitation, we think that our sample allows a statistically robust estimate of the fraction of stars formed in different bursts within GCs, with a caveat about this selection effect.

We assume the first-generation (or P) to be those stars with O and Na content similar to field stars of the same metallicity [Fe/H]. The latter are usually characterised by a pattern typical of supernova nucleosynthesis with quite uniform super-solar O values and slightly sub-solar Na abundances, the exact value depending on metallicity (with some scatter). Hence, in each

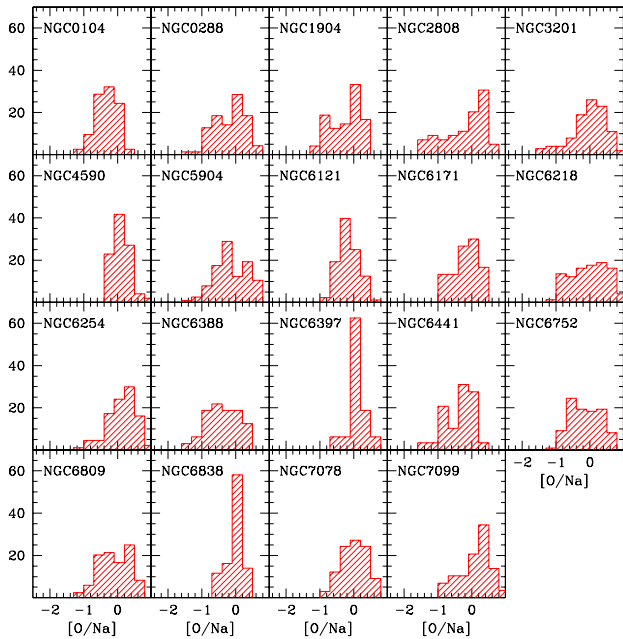


Fig. 8. Distribution function of the $[O/Na]$ ratios along the Na-O anticorrelation in all the 19 programme clusters of this project. The histograms are normalised to the total number of stars used in each cluster.

cluster, we assigned stars to the P component if their $[Na/Fe]$ ratios fall in the range within $[Na/Fe]_{\min}$ and $[Na/Fe]_{\min} + 0.3$ (that is $\sim 4\sigma([Na/Fe])$, where $\sigma([Na/Fe])$ is the star-to-star error on $[Na/Fe]$ in each cluster. The minimum value for the ratio $[Na/Fe]$ in each cluster was estimated by eye by looking at the anti correlations in Figure 7, excluding obvious outliers. They are listed in Table 7 and match the $[Na/Fe]$ ratios observed in field metal-poor stars quite well (see Section 7). With this criterion we are confident that we have included all the primordial stars, i.e. those with typical composition of normal halo stars, although a few stars with slightly modified abundances might be included, too, so this definition may somewhat overestimate the P population.

The remaining stars departing from this high-O, low-Na locus along the anticorrelation are considered all second-generation stars. We further divided this group by how much the abundances depart from those of the P population: stars with the ratio $[O/Na] > -0.9$ dex are assigned to an intermediate (I) component, while those with $[O/Na] < -0.9$ dex belong to the extreme (E) stellar component of second-generation cluster stars. We chose this separation by comparing the distribution functions of the $[O/Na]$ ratios in all clusters (see Figure 8). This limit is arbitrary and corresponds to a minimum or a sudden drop in the $[O/Na]$ distribution clearly discernible in the distribution of some clusters (NGC 2808, NGC 5904, NGC 3201), where a long tail of O-depleted stars was reliably measured. In Figure 9 the lines separating the three components are shown using NGC 5904 as an example.

We applied these criteria to all 19 our programme clusters and to the two clusters from the literature. Only the separation between the first and the second-generation stars changes, since

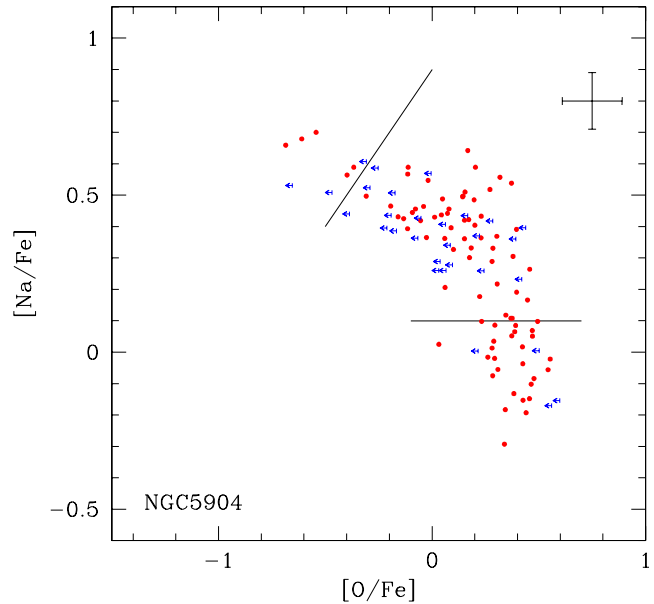


Fig. 9. The Na-O anticorrelation from our data observed in NGC 5904. The solid lines indicate the separations we adopted for the P, I, and E stellar components in this cluster.

it is tied to the minimum Na abundances that, as in field-halo stars, include a slight dependence on the metallicity. The fractions of stars in the three P, I, and E components in each cluster are listed in the last three columns of Table 5. Associated errors are computed from Poisson's statistics. In cases where no stars were found in a group (i.e., the E population), we evaluate the errors as the probability of occurrence of zero stars to be retrieved in a sample of stars (equal to the total number of stars in the anticorrelation) according to the binomial distribution.

These fractions are plotted as a function of metallicity in Figure 10, where we used cluster errors from Table 4 for our sample; for M 3 (NGC 5272) and M 13 (NGC 6205) error bars in $[Fe/H]$ are the quadratic sum of the *rms* scatters quoted in Sneden et al. (2004) and Cohen and Melendez (2005), since no systematic errors are derived in the original studies.

From the upper panel in Figure 10 it is immediately clear that a P component, which can be identified as the original, first-generation of stars, seems to be present at a constant level of about one third of the total population in *all* clusters surveyed. The average fraction we found for the set of 21 clusters is $P = 33 \pm 1\%$ with *rms* = 7% over the whole 2 dex range in metal abundance.

How statistically robust is this estimate? The three components are defined using stars in the $[Na/Fe]$ vs $[O/Fe]$ plane. However, the criterion for the P component only uses the Na abundances; hence, for this component only, we may explore the impact of adding those stars with Na but without O abundances. In our total database there are 511 objects with only Na determinations; 377 stars have no HR13 observations, the others are all quite warm (T_{eff} between 4600 and 5400 K), and metal-poor stars where the forbidden O lines can be vanish-

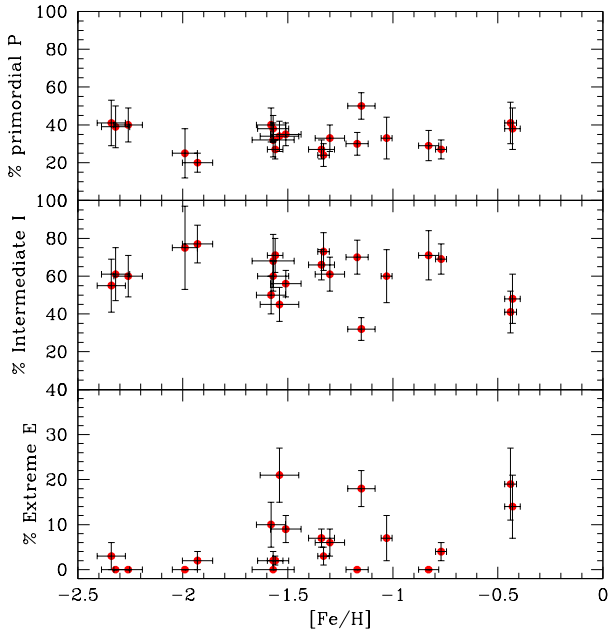


Fig. 10. Fractions of stars in the P, I, and E stellar components (upper, middle, and lower panels respectively) derived from the Na-O anticorrelation in our 19 clusters and in M 3 (NGC 5272) and M 13 (NGC 6205) from Sneden et al. (2004) and Cohen and Melendez (2005) as a function of the metallicity. Error bars in the fractions are estimated Poisson’s statistics. For metallicity we used the cluster errors (Table 4) for our sample and the quadratic sum of the *rms* scatters from the two studies for M 3 and M 13. Notice that the scale of y-axis is different in the lower panel.

ingly weak even in stars in the high-O, low-Na tail of the anticorrelation. On the other hand, Na abundances can be recovered more easily since (i) we can exploit the stronger 5682–88 Å Na I doublet for the majority of stars and (ii) the Na-depletion at this extreme is not as much as the O-depletion at the opposite end of the Na-O anticorrelation. Using this additional set of 511 stars, we computed again the fraction of the P component in our sample. Despite the increase in statistics, the new values of the P fractions changed on average by $0 \pm 1\%$ ($rms = 5\%$) for 19 clusters, but the change never exceeded 8–9%. In addition, the main statistical bias present in our data (the upper limits for O abundances in many stars) does not affect this parameter, which is only based on Na abundances. Only for the most metal-poor clusters (like M15) might we have missed the most Na-poor stars, producing some bias. In these cases Na_{min} might have been overestimated; however, the impact on the fraction on stars in the P population is small. So, we can consider the estimate of the P (first stellar generation) fraction in GCs as quite robust.

The fraction of the stars belonging to the I component (middle panel of Figure 10) would also seem about constant (at a level $\sim 65\%$) except for three clusters (NGC 2808, NGC 6388, and NGC 6441, all massive and with long blue tails on the HB) where this fraction is clearly smaller.

Finally, the fraction of component E shows the largest fluctuations, being null or very low in many clusters, raising to a modest 10% in a few, and increasing to about 20% in 4 clusters. Three of them are the objects with a lower-than-average I component seen above; to these, we can add M 13 (NGC 6205) showing an almost normal I component, but a conspicuous E stellar fraction.

On the other hand, it is not easy to assess how stable our estimates are concerning the two second-generation components (I and E), since by definition we need to know *both* Na and O abundances to assign a star to one group or to the other. Since we derived only upper limits for O abundances for a significant fraction of the stars, we might have underestimated the fractions of stars belonging to the E component; hence, should the E fraction be larger, in reality, the complementary I fraction would be smaller, by definition.

In some clusters we are quite confident that the E fraction cannot be much higher than estimated: the higher quality of data and the metallicity for 47 Tuc (NGC 104) or M 4 (NGC 6121) result in very few limits, most O determinations being actual measures. Second-generation stars with E chemical composition are simply missing in these clusters (for M 4 this is strongly supported by the recent study by Marino et al. 2008). In other cases, such as in NGC 6752, where our data are of poorer quality and we only got upper limits to O abundances for quite a large fraction of the stars, the high-resolution/high S/N data by Yong et al. (2005) show that our upper limits in O can be safely considered as actual measures and that very few or no super O-poor stars of the E component might be expected to show up in this cluster (see the discussion in Paper II).

Thus, the first conclusions we can draw from our data can be summarised as follows:

- a P population is present in all GCs; about a third of the cluster population is still made of the original first-generation, after a Hubble time since the cluster formation;
- the I component of the second-generation constitutes the bulk (50–70%) of stars in the clusters;
- E, the second-generation component with signature of extreme chemical composition is not present in all GCs.

5.3. The radial distribution of first and second-generation stars

In the Introduction, we recalled the strong existing pieces of evidence indicating that the Na-O anticorrelation is related to multiple populations in GCs. The pattern of chemical composition is the result of stellar nucleosynthesis and ejection of polluted matter. The distribution of stars along the Na-O anticorrelation may be reproduced by diluting the polluted material with pristine gas before second-generation stars form (see Prantzos, Charbonnel & Iliadis 2007). However, we still do not know whether the polluters of the first-generation contributed their enriched matter to the intra-cluster pool of gas in their main sequence phase (as fast-rotating massive stars) or in a more evolved stage (as massive AGB stars): see Decressin et al. (2007), D’Antona & Ventura (2007), Renzini (2008). However, we expect that second-generation stars should be He-rich.

Second-generation stars might be expected to form (and perhaps still be) more centrally concentrated than first-generation stars (see D’Ercole et al. 2008). In fact, the spatial distribution of first-generation stars is expected to be loose because of the cluster expansion from the large amount of mass lost by massive stars in the very early phases of cluster evolution. On the other hand, we could expect that later stellar generations form from a cooling flow at the cluster centre and are (at least initially) kinematically very cold. These different distributions should result in very different rates of evaporation, first-generation stars being lost by the cluster much more easily than second-generation ones during the early epochs of cluster evolution. On the other hand, stars with He-enhanced composition evolving off the main sequence are expected to be (slightly) less massive than those with “normal” composition (D’Antona et al. 2002). In the long dynamical evolutionary phase dominated by the two-body relaxation, the cluster is driven toward equipartition of kinetic energy. It is then possible that, after a Hubble time (and several relaxation times), He-enhanced (O-poor, Na-rich) red giants might have a more extended distribution than He-poor ones.

Very recently, Zoccali et al. (2009) have found that the peculiar second subgiant branch observed in NGC 1851 is only present in the central regions of the cluster, disappearing at about 2.4 arcmin from the cluster centre, and it is well known that the blue, He-enriched main sequence in ω Cen is more centrally concentrated than the He-normal sequence (Sollima et al. 2007).

We can test the spatial distribution of stars in the first and second generations using our database, keeping in mind the practical limitations imposed by the FPOSS positioner to the FLAMES fibres.

The cumulative radial distributions of stars in the three P, I, E components are shown in Figure 11, including the two additional clusters M 3 (NGC 5272) and M 13 (NGC 6205). Apparently, despite being forced to observe at some distance from the centre of the GCs (to maximise the number of targets in each cluster, while avoiding forbidden positions of the fibres), this figure shows that the I component is more concentrated than the P component. A Kolmogorov-Smirnov statistical test excludes that the two distributions are extracted from the same parent population, with only a 0.6% probability that this is a chance occurrence, so we remind the reader that these are the two most conspicuous components in each cluster. From the same figure it is unclear how much the E component is differently distributed with respect to the P component; from the Kolmogorov-Smirnov test, the probability that they are extracted only by chance from a same parent population is 0.7%.

However, there is the possibility that the cumulative distributions in Figure 11 are biased. In fact, although distances in different clusters are all expressed in units of half-mass radius (the region where most cluster properties are left relatively unchanged by the evolution), our programme clusters have different masses, sizes, and central concentrations; hence, we could have observed regions that are not dynamically equivalent in all clusters. This is evident in Figure 12, where we plotted the [O/Na] ratios for stars in each cluster as a function of the distance (in r_h units).

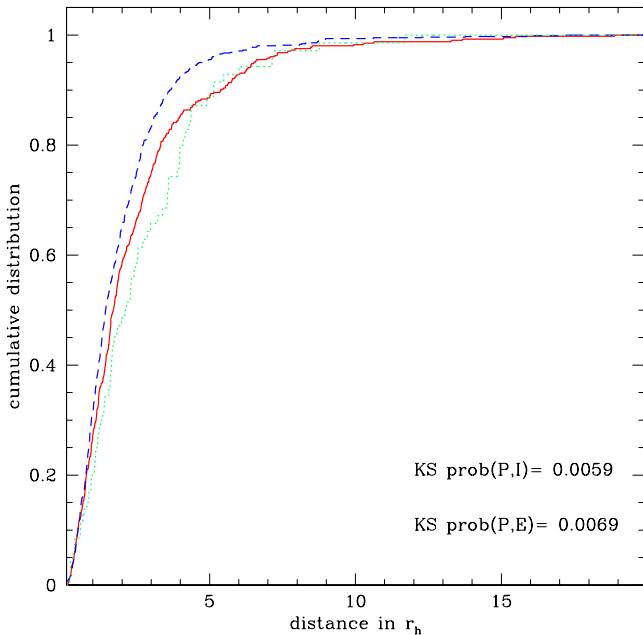


Fig. 11. Cumulative distribution of stars of the 3 components in our 19 clusters (plus M 3=NGC 5272 and M 13=NGC 6205) in unit of half-mass radii. Red solid line: component P, blue dashed line: component I, green dotted line: component E.

To check this effect we proceeded as follows. In each cluster, we computed the median of the distances from the cluster centre for each component distP_{med} , distI_{med} , and distE_{med} . Each median was normalised to that of the I population, which is the most numerous in each cluster. Afterward, we computed the average of the normalised medians for the P and E populations, and these averages are $\langle \text{distP}_{med}(\text{normalised}) \rangle = 1.329$ with $\sigma = 1.292$ and $\langle \text{distE}_{med}(\text{normalised}) \rangle = 1.151$ with $\sigma = 0.765$ from 21 and 15 clusters, respectively⁹. Although formally this might indicate that the P stars are more externally distributed, on average, than the I ones (and the E still more), the difference is not significant. The large scatter relative to the first average is all due to the value for M 3 (NGC 5272). This cluster was observed very near to the centre, because of the requirement of putting as many RGB stars as possible in the observing masks (see Sneden et al. 2004 for details). The impression is that differences in the spatial distributions of stars in the three components might exist, but they are somewhat smeared out by the bias from observing different dynamical regions in the GCs.

This impression is strengthened by Figure 13, where we plot the ratio of the fraction of P to I component as a function of the absolute visual magnitude (a proxy for the cluster mass) in the left panel and as a function of the median distance of the I component (a proxy for the typical position at which we observe the cluster, since the I stars are the bulk of the clusters’ population) in the right panel. From this figure we can see (left panel) that, by looking at more massive clusters, we observe

⁹ Obviously, $\langle \text{distI}_{med}(\text{normalised}) \rangle = 1.0$ by definition.

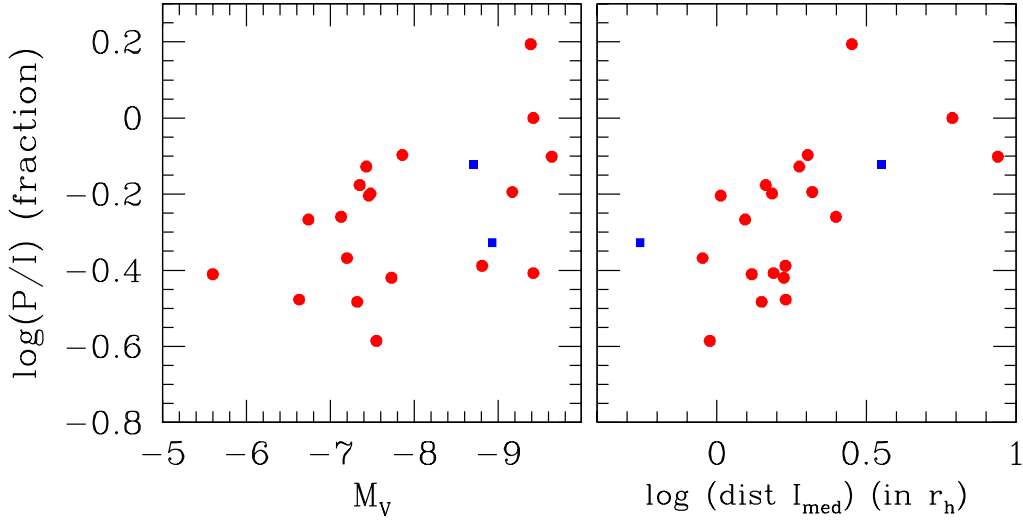


Fig. 13. The logarithm of the ratio between the fraction of stars in the P and the I components in each programme cluster as a function of the cluster total absolute visual magnitude (from Harris 1996), in the left panel, and of the median of the distances of stars in the I component from the cluster centre (in unit of half-mass radius), in the right panel. Red filled circles are our programme clusters and blue squares indicate the two additional GCs from the literature.

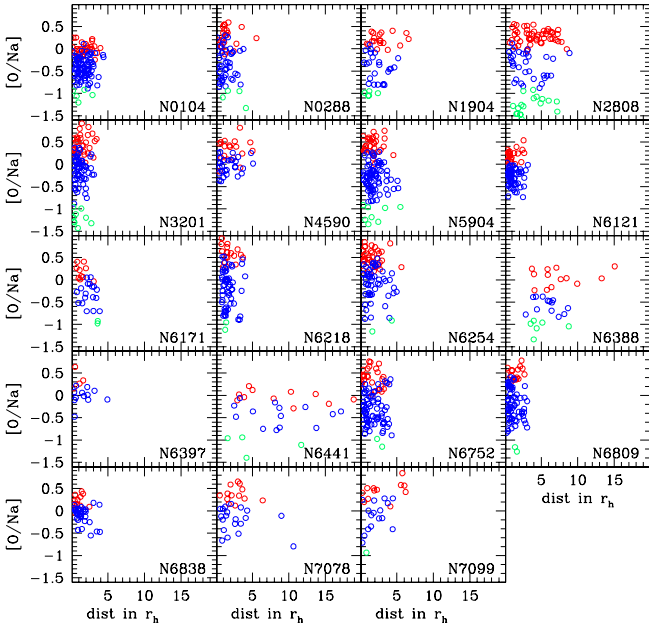


Fig. 12. [O/Na] ratios for all stars observed in our 19 programme clusters as a function of the distance from the cluster centre, expressed in units of the half-mass radius. Red, blue, and green symbols are for P, I, and E populations, respectively.

a larger fraction of P stars w.r.t. the I component. This would have a simple physical explanation because it is expected that massive objects are able to retain a larger fraction of their stars, including their first-generation stars. However, the right panel of Figure 13 shows that the P fraction is also larger in clusters

where we typically sampled more peripheral regions in the GC. The same holds had we used the ratio of P to the sum of I and E, i.e. the ratio of first to second-generation stars, without separating the two I and E components.

We can evaluate the order of magnitude of this effect by computing a “corrected” P/I ratio from the right panel of Figure 13. Although the scatter in this plot is quite large, we can fit a straight line and thus get the value of $\log(P/I)_{corr}$ that takes the position into account at which the cluster was observed (as expressed by the median of the distances of stars in the I component, in units of half-mass radius). By applying this correction we find that the ratio of P to I stars, when shifted to a reference half-mass ratio, is about constant (-0.26 in logarithm). In other words, had we always observed the bulk of our programme stars at the cluster half-mass ratio, we would have found that the P component is about 55% of the I one. Using the ratio of first to second-generation stars (the last including both I and E components) we would have found that on average from 47 to 49% of stars in clusters are from the pristine stellar generation formed in each cluster.

This exercise, while clarifying some operative issues, does not, however, solve that related to the true distribution of the three components across a GC. More observations of larger samples of stars in the smaller clusters will be needed to definitively solve the issue of the radial distribution of stars of different generations in GCs.

6. Nitrogen abundances of first and second-generation stars

The whole pattern of inter-relations among light elements in globular clusters is currently well known (see e.g. the review by Gratton et al. 2004). However, up to now, these signatures have

been poorly explored with respect to the membership of stars to one stellar generation or another in a GC. The recent paper by Marino et al. (2008) found that the dichotomy in chemistry (mainly in O, Na and N content) between two generic populations in NGC 6121 was also visible as a different photometric location along the RGB of the two groups. Using the $U - B$ colour, strongly affected by N abundances due to the location of NH (around 3360 Å) and CN (at about 3590 and 3883 Å) features, they clearly showed that Na-poor/O-rich/N-poor stars define a sequence to the blue ridge of the RGB, whereas Na-rich/O-poor/N-rich stars are more spread out, to the red of the RGB.

Calibrated Johnson U photometry is currently not available to us, but Strömgren photometry is for the programme cluster NGC 6752. We cross-identified our sample in this cluster with unpublished Strömgren photometry (Grundahl 1999, private communication), finding 42 stars in common. In the left panel of Figure 14, these stars are plotted in the Strömgren $u, u - b$ CMD, with different symbols according to the division in stellar populations in the previous section. We can see that the five stars of the first stellar generation (P component) define a very tight sequence on the left ridge of the RGB, while the other stars (all belonging to the I component) populate the remaining of the giant branch with a larger dispersion. This is *not* a temperature effect, due to systematic differences in the effective temperature of first and second generation stars, as can be inferred from the middle and right panels in Figure 14. In the $u, V - K$ the separation of the two sequence is less clear, and in the more classical $V, V - K$ CMD they are virtually indiscernible.

Other evidence comes from the two Strömgren indexes c_1 and c_y . Yong et al. (2008) defined an empirical index c_y designed to trace N abundances (its definition includes c_1 , which in turn uses the u filter, where the effect of the NH band is stronger), but removing temperature effects from the classical index c_1 . In Figure 15 we superimpose the first and second-generation stars we found in NGC 6752 (defined only from their abundances of Na) on the diagrams from the whole Strömgren unpublished photometry for this cluster, using both the c_1 index (left panel) and the newly defined c_y index, reproducing the same plots as in Yong et al. (2008, their Figures 1 and 6).

Again, P stars define a very tight sequence, as expected for stars born in a single burst of star formation in the still unpolluted environment of the early GC. On the other hand, the I component shows a much larger dispersion in both indexes, as expected from stars born from matter resulting from a variable mix of ejecta enriched in products of H-burning at high temperature and pristine unpolluted gas.

Finally, we can estimate the typical N content associated to the P and I populations by using the empirical calibration given in Yong et al. (2008) and derived exactly in NGC 6752. The results for our stars of NGC 6752 are displayed in Figure 16, where the error bar in $[N/Fe]$ is the *rms* scatter of the relation between $[N/Fe]$ and c_y quoted by Yong and collaborators (0.29 dex). The average value of $[N/Fe]$ for the P component is about solar, $[N/Fe] = -0.04$ dex ($\sigma = 0.17$ dex, 5 stars); for

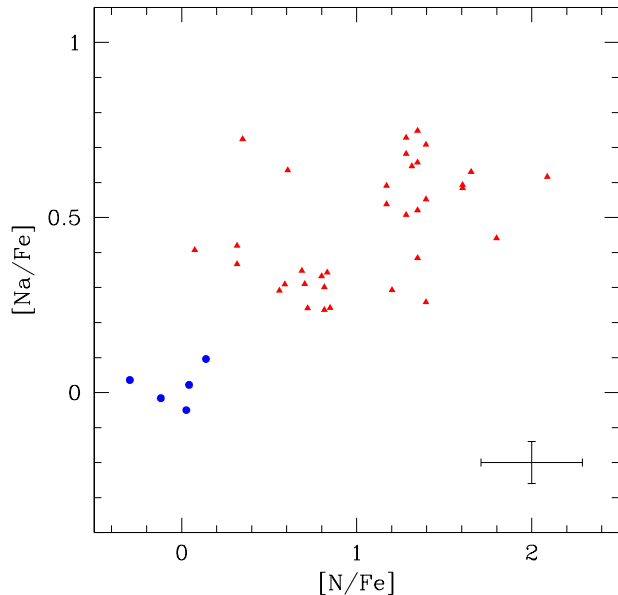


Fig. 16. Abundances of Na from our analysis (Paper II) vs $[N/Fe]$ ratios derived from the calibration by Yong et al. (2008) of the index c_y for 42 stars in NGC 6752 with Strömgren photometry. Errors bars are from Paper II (for Na) and from the *rms* scatter of the relation by Yong et al. (2008). Blue filled circles are stars of the P component and red triangles are stars of the I component.

the I component, we derive a much higher average value of $[N/Fe] = +1.00$ dex and a large scatter ($\sigma = 0.50$ dex, 37 stars).

7. A dilution model for the Na-O anticorrelation and the shape of the Na-O anticorrelation

We do not have a satisfactory model yet for the mechanism responsible of the Na-O anticorrelation, and even the astrophysical site is currently debated (fast-rotating massive stars vs massive AGB stars undergoing hot bottom burning: see Decressin et al. 2007; Ventura et al. 2001). A simple approach is to assume (i) that within each cluster there is a unique mechanism that produces some given amount of sodium and destroys almost all O (transforming it into N); and (ii) that the processed material is then mixed with a variable amount of pristine material. A similar dilution model has been successfully used to explain many features of the Na-O anticorrelation (see discussion in Prantzos et al. 2007). Once the compositions of the pristine and processed material are set (e.g., by the extremes of the observed distributions), an appropriate dilution factor may be determined for each star (either from O or Na abundances).

In this model the logarithmic abundance of an element $[X]$ for a given dilution factor *dil* is given by:

$$[X] = \log [(1 - dil) 10^{[X_o]} + dil 10^{[X_p]}], \quad (1)$$

where $[X_o]$ and $[X_p]$ are the logarithmic abundance of the element in the original and processed material. In principle, $[X_o]$

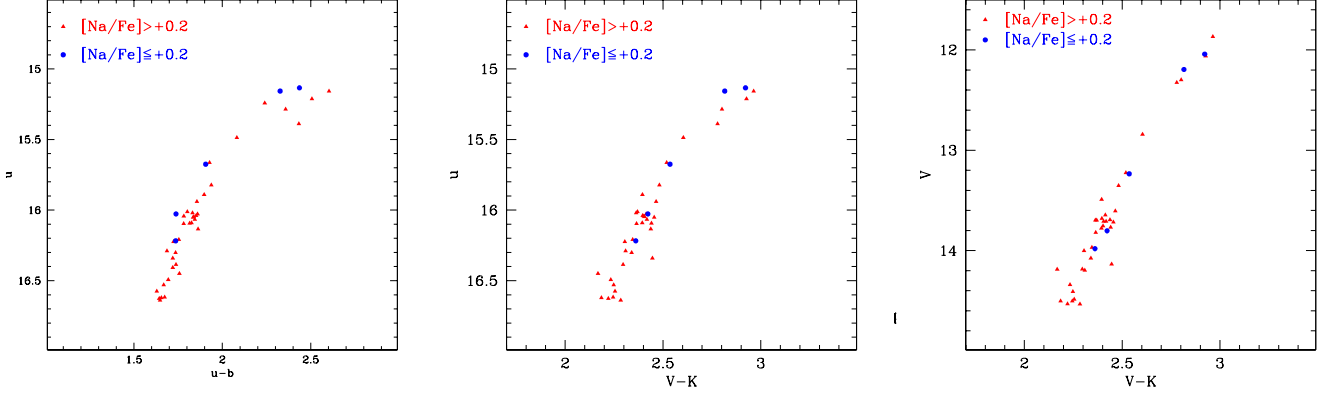


Fig. 14. Left panel: Strömgren u vs $u - b$ CMD for the 42 stars in NGC 6752 in common with the unpublished photometry by Grundahl et al. (1999). Middle panel: the same, but using the $V - K$ colour as abscissa. Right panel: V vs $V - K$ CMD. In all panels blue filled circles indicate first-generation stars (P component) and red triangles second-generation stars (I component) in NGC 6752.

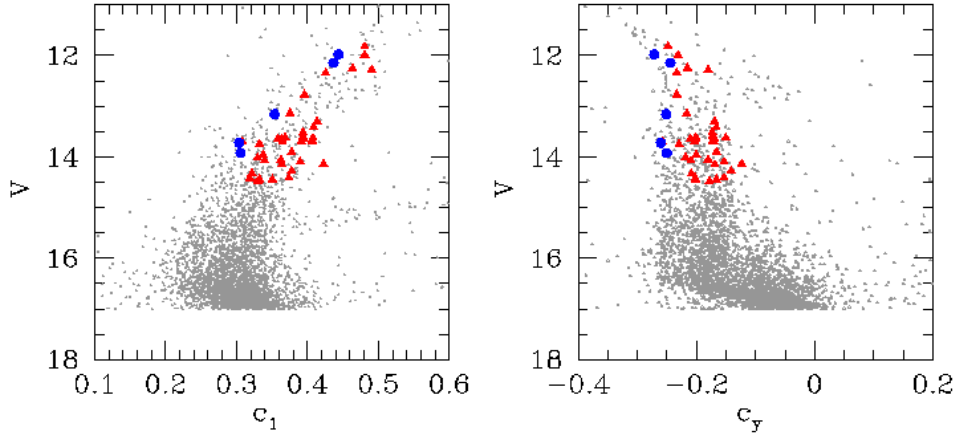


Fig. 15. Left and right panels: the V vs c_1 and V vs c_y , respectively, CMDs, as in Yong et al. (2008) using for NGC 6752 the unpublished photometry by Grundahl et al. (1999). Filled (blue) circles and (red) triangles are stars of the first and second-generations, respectively, as defined in this work on the basis of their Na abundances alone.

and $[Xp]$ could be derived from observations for both O and Na. We may adopt for $[Xo]$ the maximum observed abundance of O ($[O/Fe]_{\max}$) and the minimum observed abundance of Na ($[Na/Fe]_{\min}$), and for $[Xp]$ the minimum observed abundance of O ($[O/Fe]_{\min}$) and the maximum observed abundance of Na ($[Na/Fe]_{\max}$). Practically, we derived minimum O and Na abundances by visual inspection of the observed distributions, while we obtained the maximum Na and O abundances by minimising the r.m.s. of points due to individual stars along dilution fitting relations¹⁰. Table 7 gives the minimum and maximum O and Na abundances we obtained for the 19 clusters in our programme. In many cases we can only derive upper limits

to $[O/Fe]_{\min}$. This is surely the case for the most metal-poor GCs ($[Fe/H] < -1.7$), where we may grossly overestimate the $[O/Fe]_{\min}$. We explicitly indicate this in the second column of Table 7. Also, $[Na/Fe]_{\min}$ can be overestimated for the most metal-poor GCs, which we think this may be the case for M15 (NGC 7078).

As mentioned above, the minimum Na and maximum O abundances in each cluster represent the original Na and O composition of the cluster. It is interesting to plot their runs with $[Fe/H]$ and to compare them with the runs observed in field halo stars (see Fig. 17). The upper panel of this figure indicates that GCs generally started from high values of the O abundances of $[O/Fe] \sim 0.35 \div 0.5$, implying a marginal contribution (if any) by type Ia SNe to their original composition. Only the two most metal-rich clusters (NGC 6388 and NGC 6441), both at $[Fe/H] \sim -0.4$, have a moderate excess of

¹⁰ When doing this exercise, we considered upper limits as actual detections. Also, in the case of NGC 6441 we neglected the two stars with the largest Na abundances, which clearly stand out with respect to the relation given by the other stars.

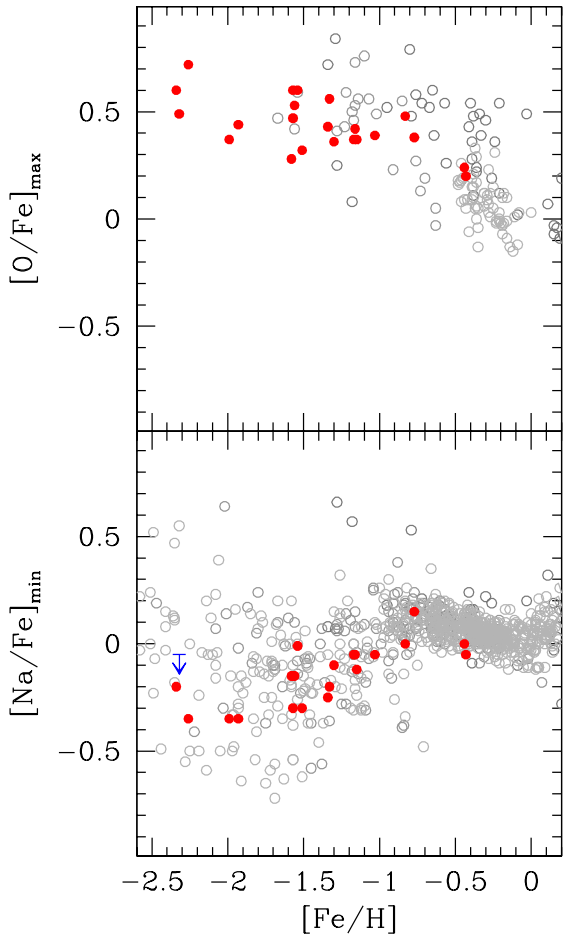


Fig. 17. Run of $[O/Fe]_{\max}$ (upper panel) and $[Na/Fe]_{\min}$ (lower panel) with $[Fe/H]$ for the GCs of our sample. These should represent the run of original O and Na abundances for these clusters. The grey, open symbols, represent field stars taken from Fulbright, McWilliam & Rich (2007), Venn et al. (2004), Gratton et al. (2003), Reddy et al. (2003).

Table 7. Minimum and maximum abundances of O and Na from our dilution model

NGC	$[O/Fe]_{\min}$	$[Na/Fe]_{\min}$	n	$[O/Fe]_{\max}$	$[Na/Fe]_{\max}$	rms
104	-0.4	0.15	114	0.38 ± 0.08	0.74 ± 0.06	0.08
288	-0.5	-0.10	70	0.36 ± 0.18	0.71 ± 0.18	0.18
1904	-0.6	-0.15	48	0.28 ± 0.09	0.72 ± 0.07	0.10
2808	-1.0	-0.12	98	0.37 ± 0.07	0.56 ± 0.04	0.10
3201	-0.8	-0.30	100	0.32 ± 0.10	0.60 ± 0.09	0.15
4590	< 0.0	-0.35	48	0.72 ± 0.20	0.53 ± 0.13	0.13
5904	-0.7	-0.25	124	0.43 ± 0.13	0.60 ± 0.10	0.14
6121	-0.2	-0.05	88	0.37 ± 0.07	0.74 ± 0.08	0.07
6171	-0.3	-0.05	30	0.39 ± 0.09	0.69 ± 0.07	0.08
6218	-0.4	-0.20	74	0.56 ± 0.11	0.67 ± 0.07	0.13
6254	-0.4	-0.30	87	0.47 ± 0.09	0.56 ± 0.10	0.12
6388	-0.6	0.00	32	0.24 ± 0.11	0.67 ± 0.05	0.10
6397	< 0.0	-0.35	16	0.37 ± 0.09	0.71 ± 0.23	0.06
6441	-0.4	-0.05	27	0.20 ± 0.11	0.80 ± 0.10	0.12
6752	-0.4	-0.15	98	0.53 ± 0.13	0.65 ± 0.07	0.14
6809	< -0.2	-0.35	84	0.44 ± 0.14	0.69 ± 0.09	0.12
6838	0.0	0.00	42	0.48 ± 0.10	0.76 ± 0.16	0.09
7078	< -0.1	< -0.05	33	0.49 ± 0.09	0.70 ± 0.09	0.09
7099	< -0.2	-0.20	29	0.60 ± 0.15	0.76 ± 0.14	0.14

O ($[O/Fe] \sim 0.2$): these clusters are well beyond the knee of the $[O/Fe]$ run observed for field stars. Also the run for $[Na/Fe]_{\min}$ with $[Fe/H]$ closely reflects that observed among metal-poor stars. We conclude that the original composition of GCs reflected the typical composition of the field halo material.

The minimum O and maximum Na abundances in each cluster determine the slope of the O/Na anticorrelation. If the polluters were massive AGB stars, these two quantities would be expected to be anticorrelated, depending on the average mass and metallicity of the polluters; hence, $[O/Fe]_{\min}$ and $[Na/Fe]_{\max}$ might change from cluster to cluster. This is indeed the case: for instance, NGC 2808, with $[Na/Fe]_{\max} = 0.58 \pm 0.03$ has a O/Na anticorrelation clearly flatter than M 4 ($[Na/Fe]_{\max} = 0.70 \pm 0.11$; see Figure 18), in spite of the fact that these two clusters have very similar values of $[Fe/H]$. This suggests that the average mass of the polluters may be larger in NGC 2808 than in M 4. Searching for general trends, we plotted the run of $[Na/Fe]_{\max}$ with $[O/Fe]_{\min}$ in Figure 19. If we neglect the upper limits (which do not provide useful information here), we find that these two quantities are correlated, as expected for massive AGB polluters. However, the observed slope is quite different from model expectations, the variation in $[O/Fe]_{\min}$ being much greater than expected. This might indicate some flaws in the model (e.g. in the treatment of convection and/or on the adopted value for the relevant nuclear reaction cross sections). However (still excluding the most metal-poor clusters, which only provide not very constraining upper limits), we find that $[O/Fe]_{\min}$ is closely correlated with a linear combination of metallicity $[Fe/H]$ and cluster luminosity M_V , the mean relation being

$$[O/Fe]_{\min} = (0.366 \pm 0.134)[Fe/H] + (0.168 \pm 0.044)M_V + (1.23 \pm 0.17), \quad (2)$$

with a linear correlation coefficient of $r = 0.77$ (over 14 GCs), which is highly significant (see also Figure 20). The correlation with the cluster absolute magnitude suggests that the average mass of the polluting stars is correlated with the cluster's absolute magnitude (or, more likely, with the mass of the cluster at the epoch of formation, of which its current M_V value can be a proxy). It is unfortunate that current AGB models are not yet able to provide a good calibration of the polluting mass, because this would provide us with the typical timescale for the formation of the second-generation, a crucial piece of information in modelling early phases of cluster evolution.

8. Summary

In this paper we have derived atmospheric parameters and elemental abundances of iron, oxygen, and sodium for 1582 *bona fide* member red giant stars in 15 Galactic GCs with different global parameters (metallicity, masses, HB morphology, etc.). We derived our abundances from *EWs* measured on high-resolution FLAMES/GIRAFFE spectra; the *EWs* are corrected to a system defined by higher resolution FLAMES/UVES spectra (presented in the companion Paper VIII). We added stars analysed in the previous studies within the project to the sample of the present paper, and the resulting sample was completed with the UVES dataset. We have a grand total of 1235 stars with homogeneous Na and O abundances in 19 clusters,

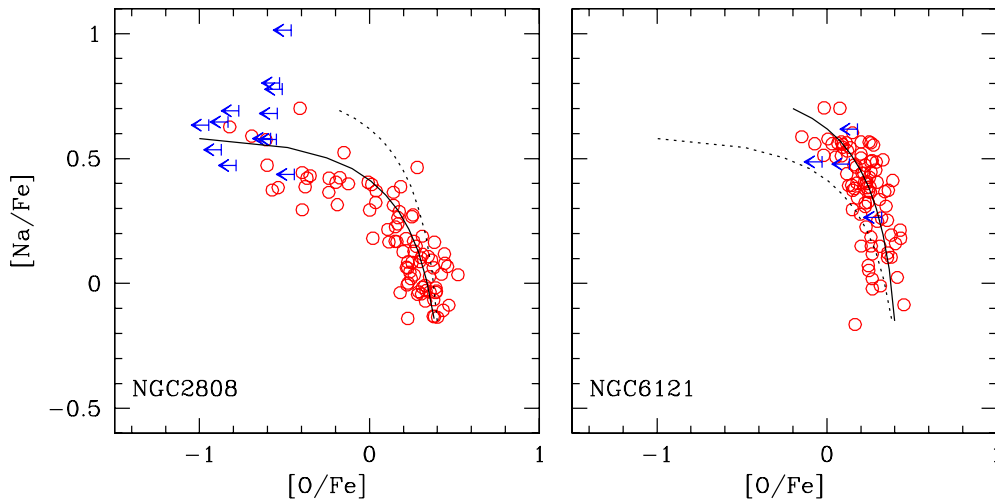


Fig. 18. The O/Na anticorrelation in NGC 2808 (left panel) and M 4 (NGC 6121, right panel). Red circles represent stars with actual measures of the O abundances, while blue arrows represent those stars for which only upper limits were obtained. Overlying lines are the results of our dilution model for the two clusters, respectively.

the largest sample of its kind ever collected. This huge database allows tracing the Na-O anticorrelation for each GC, the typical signature of operation of proton-capture chains in high-temperature H-burning in an early generation of -now extinct-massive stars. This classical sign of large star-to-star abundance variations *is present in all clusters studied to date, so it must be fundamentally related to the mechanisms of formation and early evolution of GCs*. For some of the clusters in our sample the Na-O anticorrelation is detected here for the first time.

Our homogeneous abundances are used to provide a chemically tag of multiple stellar populations and allow us to separate and *quantify* the fraction of first and second-generation stars in globular clusters. A component P is identified with stars populating (in the Na-O plane) the locus occupied by field stars of similar metallicity, showing only the chemical pattern from supernovae nucleosynthesis. This P component is present in all clusters, at a level averaging from about 30 up to (in a few cases) 50% : no cluster is found completely lacking the pristine stellar component. This is at variance with the suggestion (D’Antona and Caloi 2008) that some clusters (e.g. NGC 6397) are only composed of second-generation stars.

The remaining stars are second-generation stars, formed by the gas pool polluted by intermediate and/or massive first-generation stars. According to the degree of changes in O and Na, we could separate this second-generation into an I and E populations. The I component represents the bulk of the clusters’ present population, including up to 60-70% of currently observed cluster stars. The E population is not present in all clusters and is more easily found in very massive clusters. However, this is a necessary but not sufficient condition: massive clusters such as 47 Tuc (NGC 104) and maybe M 15 (NGC 7078) do not harbour a significant fraction of stars with heavily modified chemical composition.

We found a tendency for I stars to be more concentrated toward the cluster centre than P stars, but the significance of

this finding might be somewhat biased by our likely observing dynamically different regions in different clusters (due to the combination of cluster parameters and size on the sky and to the mechanical limitations of the fibre positioner of FLAMES). Although there are hints of a different spatial distribution of the three P,I,E cluster populations, further observations and larger samples of stars are needed, especially in the smaller clusters.

Using Strömgen photometry we verified in NGC 6752 that stars of the first-generation are also N-poor, while stars of the second-generation (the intermediate component) are N-rich. The N content affects blue colours (such as the $u - b$) through the u band flux; this causes the P stars to lie along a tight sequence on the blue of the RGB, while the I stars, composed of a mix of polluted, N-enriched matter, and of pristine gas, populate a wider part of the CMD.

Finally, the comparison of the observed Na-O anticorrelation with dilution sequences has allowed us to (i) determine the original O and Na abundances; (ii) show that these anticorrelations differ systematically from cluster to cluster, the maximum Na and minimum O abundances being correlated, in qualitative but not quantitative agreement with nucleosynthesis prediction for massive AGB stars; and (iii) find that the slope of the Na-O anticorrelation is driven by metallicity and cluster absolute magnitude (or mass). When compared with the nucleosynthesis predictions, this suggests that the average mass of polluting stars is anticorrelated with total cluster mass.

Acknowledgements. This publication makes use of data products from the Two Micron All Sky Survey, which is a joint project of the University of Massachusetts and the Infrared Processing and Analysis Center/California Institute of Technology, funded by the National Aeronautics and Space Administration and the National Science Foundation. This work was partially funded by the Italian MIUR under PRIN 2003029437. We also acknowledge partial support from the grant INAF 2005 “Experimenting nucleosynthesis in clean environments”. We warmly thank the referee, Mike Bessell, for the careful

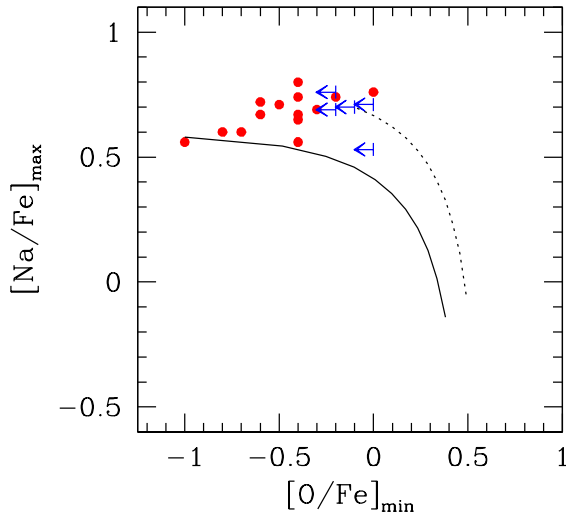


Fig. 19. Run of $[\text{Na}/\text{Fe}]_{\text{max}}$ with $[\text{O}/\text{Fe}]_{\text{min}}$ for the GCs of our sample. Arrows represent upper limits and the two lines are the dilution relations for NGC 2808 and NGC 6121 shown in the previous figure.

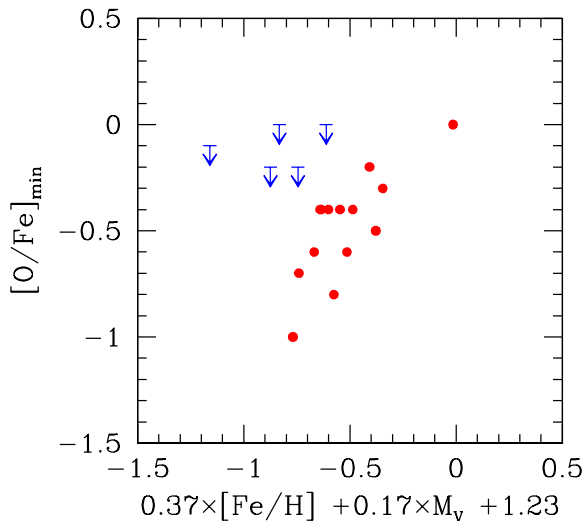


Fig. 20. Run of $[\text{O}/\text{Fe}]_{\text{min}}$ for the GCs of our sample as a function of a linear combination of metallicity $[\text{Fe}/\text{H}]$ and cluster luminosity M_V . This relation was computed by excluding the five most metal-poor GCs, indicated by arrows.

reading of this manuscript and for his suggestions improving the paper. S.L. is grateful to the DFG cluster of excellence ‘‘Origin and Structure of the Universe’’ for partial support. M.B. acknowledges the financial support of INAF through the PRIN-2007 grant CRA 1.06.10.04. We also wish to thank F. De Angeli for preparatory work and C. Corsi, L. Pulone, and F. Grundahl for their unpublished photometry. This research has made use of the SIMBAD database, operated at CDS, Strasbourg, France and of NASA’s Astrophysical Data System.

References

- Alonso, A., Arribas, S. & Martinez-Roger, C. 1999, *A&AS*, 140, 261
 Alonso, A., Arribas, S. & Martinez-Roger, C. 2001, *A&A*, 376, 1039
 Asplund, M., Nordlund, Å., Trampedach, R., & Stein, R. F. 1999, *A&A*, 346, L17
 Bellazzini, M., Fusi Pecci, F., Ferraro, F.R., Galletti, S., Catelan, M., Landsman, W.B. 2001, *AJ*, 122, 2569
 Bragaglia, A., Carretta, E., Gratton, R.G. et al. 2001, *AJ*, 121, 327
 Briley, M.M., Cohen, J.G., Stetson, P.B. 2004, *AJ*, 127, 1579
 Cannon, R.D., Croke, B.F.W., Bell, R.A., Hesser, J.E., Stathakis, R.A. 1998, *MNRAS*, 298, 601
 Cardelli, J.A., Clayton, G.C., & Mathis, J.S. 1989, *ApJ*, 345, 245
 Carretta, E. 2006, *AJ*, 131, 1766
 Carretta, E., Bragaglia, A. & Cacciari 2004b, *ApJ*, 610, L25
 Carretta, E., Bragaglia, A., Gratton R.G., Leone, F., Recio-Blanco, A., Lucatello, S. 2006a, *A&A*, 450, 523 (Paper I)
 Carretta, E., Bragaglia, A., Gratton R.G., Lucatello, S., & Momany, Y. 2007a, *A&A*, 464, 927 (Paper II)
 Carretta, E., Gratton R.G., Bragaglia, A., Bonifacio, P. & Pasquini, L. 2004a, *A&A*, 416, 925
 Carretta, E. et al. 2007b, *A&A*, 464, 967 (Paper VI)
 Carretta, E. et al. 2007c, *A&A*, 464, 939 (Paper IV)
 Cassisi, S., Bragaglia, A., Gratton, R., Milone, A., Piotto, G., Renzini, A. 2008, *The Messenger* (supplement), 134, 13
 Cohen, J.G., Melendez, J. 2005, *AJ*, 129, 303
 Cudworth, K.M. 1976, *AJ*, 81, 519
 Cudworth, K.M. 1979, *AJ*, 84, 1866
 Cudworth, K.M. 1985, *AJ*, 90, 65
 Cudworth, K.M., & Rees, R. 1990, *AJ*, 99, 1491
 Cudworth, K.M., Smetanka, J.J., & Majewski, S.R. 1992, *AJ*, 103, 1252
 D’Antona, F. & Caloi, V. 2008, *MNRAS*, 390, 693
 D’Antona, F., Caloi, V., Montalbán, J., Ventura, P., Gratton, R. 2002, *A&A*, 395, 69
 D’Antona, F., Ventura, P. 2007, *MNRAS*, 379, 1431
 D’Ercole, A., Vesperini, E., D’Antona, F., McMillan, S.L.W., Recchi, S. 2008, *MNRAS*, 391, 825
 Decressin, T., Meynet, G., Charbonnel, C., Prantzos, N., Ekstrom, S. 2007, *A&A*, 464, 1029
 Denisenkov, P.A., Denisenkova, S.N. 1989, *A.Tsir.*, 1538, 11
 Fitzpatrick, E.L. 1999, *PASP*, 111, 63
 Fullbright, J.P., McWilliam, A., Rich, M.R. 2007, *ApJ*, 661, 1152
 Gratton, R.G., Bonifacio, P., Bragaglia, A., et al. 2001, *A&A*, 369, 87
 Gratton, R.G., Carretta, E., Claudi, R., Lucatello, S., & Barbieri, M. 2003, *A&A*, 404, 187
 Gratton, R.G., Carretta, E., Eriksson, K., & Gustafsson, B. 1999, *A&A*, 350, 955
 Gratton, R.G., Lucatello, S., Bragaglia, A., Carretta, E., Momany, Y., Pancino, E., Valenti, E. 2006, *A&A*, 455, 271 (Paper III)
 Gratton, R.G., Sneden, C., & Carretta, E. 2004, *ARA&A*, 42, 385
 Gratton, R.G., Sneden, C., Carretta, E., & Bragaglia, A. 2000, *A&A*, 354, 169
 Gratton, R.G. et al. 2007, *A&A*, 464, 953 (Paper V)
 Grundahl, F., Vandenberg, D.A., Stetson, P.B., Anderson, M.I., Briley, M. 1999, in *The Galactic Halo: from GCs to field stars* [astro-ph/9909447]
 Harris, W. E. 1996, *AJ*, 112, 1487
 Kraft, R.P. 1994, *PASP*, 106, 553
 Kurucz, R.L. 1993, CD-ROM 13, Smithsonian Astrophysical
 Landolt, A.U. 1992, *AJ*, 104, 340
 Langer, G.E., Hoffman, R., & Sneden, C. 1993, *PASP*, 105, 301
 Magain, P. 1984, *A&A*, 134, 189
 Mackey A.D., van den Bergh, S. 2008, *MNRAS*, 360, 631

- Marino, A. Villanova, S., Piotto, G., Milone, A.P., Momany, Y., Bedin, L.R., Medling, A.M. 2008, A&A, 490, 625
- Momany, Y., Bedin, L.R., Cassisi, S., Piotto, G., Ortolani, S., Recio-Blanco, A., De Angeli, F., & Castelli, F. 2004, A&A, 420, 605
- Momany, Y., Cassisi, S., Piotto, G., Bedin, L.R., Ortolani, S., Castelli, F., & Recio-Blanco, A. 2003, A&A, 407, 303
- Pasquini, L. et al. 2002, The Messenger, 110, 1
- Piotto, G. 2009, in "Ages of Stars", IAU Symp. 258, in press (arXiv:0902:1422)
- Prantzos, N., Charbonnel, C., Iliadis, C. 2007, A&A, 470, 179
- Ramirez, S., Cohen, J.G. 2002, AJ, 123, 3277
- Reddy, B.E., Tomkin, J., Lambert, D.L., Allende prieto, C. 2003, MNRAS, 340, 304
- Renzini, A. 2008, MNRAS, 391, 354
- Sandquist, E.L., Bolte, M., Stetson, P.B., Hesser, J.E. 1996, ApJ, 470, 910
- Schechter, P.L., Huchra, J.P., Tonry, J.L. 1993, PASP, 105, 1470
- Skrutskie, M.F. et al. 2006, AJ, 131, 1163
- Smith, V.V., Cunha, K., Ivans, I.I., Lattanzio, J.C., Campbell, S. 2005, ApJ, 633, 392
- Smith, G.H., Martell, S.L. 2003, PASP, 115, 1211
- Snedden, C., Kraft, R.P., Guhathakurta, P., Peterson, R.C., Fulbright, J.P. 2004, AJ, 127, 2162
- Sollima, A., Ferraro, F.R., Bellazzini, M., Origlia, L., Straniero, O., Pancino, E. 2007, ApJ, 654, 915
- Stetson, P.B. 1994, PASP, 106, 250
- Stetson, P.B. 2000, PASP, 112, 925
- Yong, D., Grundahl, F., Johnson, J.A., Asplund, M. 2008, ApJ, 684, 1159
- Yong, D., Grundahl, F., Nissen, P.E., Jensen, H.R., Lambert, D.L. 2005, A&A, 438, 875
- Zoccali, M., Pancino, E., Catelan, M., Hempel, M., Rejkuba, M., Carrera, R. 2009, ApJL, in press (arXiv:0901.4476)
- Venn, K.A., Irwin, M., Shetrone, M.D., Tout, C.A., Hill, V., Tolstoy, E. 2004, AJ, 128, 1177
- Ventura, P. D'Antona, F., Mazzitelli, I., & Gratton, R. 2001, ApJ, 550, L65

Appendix A: Error estimates

A.1. Individual (star-to-star) errors

In the following discussion we focus our attention on individual (i.e. star-to-star) errors in the derived abundances that are relevant when discussing the internal spread of abundance within a cluster, which is our main aim. As shown in previous works (see e.g. Paper IV, Paper V), the main error sources are those in temperature, microturbulent velocity and *EWs*. The effects of errors in surface gravities and in the adopted model metallicity are negligible in the total error budget.

The error estimate can be split into 3 steps.

Sensitivities of abundance ratios to atmospheric parameters.

The first step in our error analysis is to evaluate the sensitivity of the derived abundances to the adopted atmospheric parameters. These sensitivities were obtained by repeating our abundance analysis by changing only one atmospheric parameter each time.

Notice that *at least* two typical cases (a cool and a warm star) are required, because cool and warm stars are in two different regimes, in warm stars Fe is mainly ionised, while in cool

stars Fe is mainly neutral. For this reason, sensitivities to variations in effective temperatures and surface gravities are different in the two cases. In our case, this exercise was done on *all* the stars in each cluster. Afterward, we adopt the sensitivity in each parameter as the one corresponding to the average of all the sample (separately for each cluster).

The amount of the variations in the atmospheric parameters and the resulting response in abundance changes of Fe, O, and Na (the sensitivities) are shown in Table A.1.

Errors in atmospheric parameters The next step is to evaluate the actual errors in the atmospheric parameters. The individual star errors are those that show up when we compare abundances obtained from different stars in the same cluster. A detailed and more wordy discussion of how they can be estimated is given in Paper IV; here we only provide a schematic description. Results are given in columns labelled 2 to 6 of Table A.2.

- internal error in T_{eff} are estimated from the slope of the relation between $T_{\text{eff}}(V-K)$ from the Alonso et al. calibration and the V or K magnitude, assuming an error of 0.02 mag.
- the error in the micro-turbulent velocity is estimated by the change in v_t required to vary the slope of the expected line strength vs abundances relation by 1σ ; this value was derived as the quadratic mean of the 1σ errors in the slope of the relation between abundance and expected line strength for all stars with enough Fe I lines measured.
- to estimate errors in the measurement of *EWs* we selected a subset of stars with more than 15 measured Fe lines in each cluster (this number dropped down to 10 or 6 for the most metal-poor clusters). The average *rms* scatter in Fe abundance for these stars, divided by the square root of the typical average number of measured lines, provides the typical internal errors listed in Table A.2, column label (5).

Estimate of error in abundances Once estimates of the individual star errors in the atmospheric parameters are available (Table A.2), they may be multiplied for the sensitivities of abundances to variations in the individual parameters (Table A.1) to derive their contribution to the total individual star errors, listed in Tab A.3.

Total errors, computed by summing in quadrature only the dominant terms (due to T_{eff} , v_t and *EWs*), or including all the contributions, are reported in Table A.3, in Cols. 8 and 9 respectively, for iron and for the other two elements O and Na. From this table one can also appreciate how negligible is to include of error sources due to gravity and model metal abundance.

In almost all clusters the observed scatter (col. 5 in Table 4) is formally lower than the total star-to-star error, which might indicate that the errors are slightly overestimated.

In summary, our abundance analysis and error estimate allow us to conclude that each of the clusters of the present project shows a high degree of homogeneity as far as the global metallicity is concerned, since we do not find any statistically significant intrinsic spread in [Fe/H].

Table A.1. Sensitivities of abundance ratios to errors in the atmospheric parameters

cluster	$\Delta T_{\text{eff}} = 50 \text{ K}$				$\Delta V_t = +0.1 \text{ km/s}$			
	$\Delta[\text{Fe}/\text{H}]_{\text{I}}$	$\Delta[\text{Fe}/\text{H}]_{\text{II}}$	$\Delta[\text{O}/\text{Fe}]$	$\Delta[\text{Na}/\text{Fe}]$	$\Delta[\text{Fe}/\text{H}]_{\text{I}}$	$\Delta[\text{Fe}/\text{H}]_{\text{II}}$	$\Delta[\text{O}/\text{Fe}]$	$\Delta[\text{Na}/\text{Fe}]$
NGC 104	+0.033	-0.049	-0.025	+0.009	-0.034	-0.016	+0.035	+0.008
NGC 288	+0.055	-0.026	-0.044	-0.016	-0.027	-0.012	+0.029	+0.018
NGC 1904	+0.060	-0.022	-0.042	-0.022	-0.027	-0.008	+0.029	+0.021
NGC 3201	+0.059	-0.022	-0.044	-0.021	-0.022	-0.009	+0.024	+0.020
NGC 4590	+0.049	-0.007	-0.023	-0.023	-0.011	-0.005	+0.014	+0.009
NGC 5904	+0.057	-0.029	-0.043	-0.016	-0.028	-0.011	+0.028	+0.019
NGC 6121	+0.049	-0.034	-0.038	-0.006	-0.031	-0.011	+0.033	+0.018
NGC 6171	+0.045	-0.037	-0.035	-0.002	-0.026	-0.013	+0.028	+0.015
NGC 6254	+0.055	-0.014	-0.037	-0.021	-0.018	-0.006	+0.020	+0.015
NGC 6388	+0.015	-0.073	-0.006	+0.023	-0.044	-0.023	+0.045	+0.014
NGC 6397	+0.047	-0.007	-0.034	-0.021	-0.009	-0.003	+0.010	+0.009
NGC 6808	+0.062	-0.016	-0.042	-0.028	-0.015	-0.004	+0.017	+0.012
NGC 6838	+0.052	-0.038	-0.046	-0.011	-0.032	-0.016	+0.033	+0.013
NGC 7078	+0.050	-0.011	-0.026	-0.023	-0.008	-0.002	+0.011	+0.007
NGC 7099	+0.047	-0.010	-0.021	-0.021	-0.008	-0.002	+0.010	+0.006

cluster	$\Delta \log g = +0.2 \text{ dex}$				$\Delta [\text{A}/\text{H}] = +0.1 \text{ dex}$			
	$\Delta[\text{Fe}/\text{H}]_{\text{I}}$	$\Delta[\text{Fe}/\text{H}]_{\text{II}}$	$\Delta[\text{O}/\text{Fe}]$	$\Delta[\text{Na}/\text{Fe}]$	$\Delta[\text{Fe}/\text{H}]_{\text{I}}$	$\Delta[\text{Fe}/\text{H}]_{\text{II}}$	$\Delta[\text{O}/\text{Fe}]$	$\Delta[\text{Na}/\text{Fe}]$
NGC 104	+0.015	+0.107	+0.070	-0.054	+0.009	+0.037	+0.027	-0.001
NGC 288	-0.009	+0.087	+0.090	-0.025	-0.007	+0.020	+0.034	-0.004
NGC 1904	-0.011	+0.083	+0.090	-0.025	-0.010	+0.018	+0.036	-0.005
NGC 3201	-0.009	+0.084	+0.089	-0.019	-0.009	+0.021	+0.038	-0.001
NGC 4590	-0.005	+0.073	+0.079	-0.015	-0.003	+0.005	+0.016	+0.003
NGC 5904	-0.005	+0.087	+0.086	-0.029	-0.007	+0.022	+0.037	-0.007
NGC 6121	-0.004	+0.093	+0.089	-0.033	-0.002	+0.025	+0.034	-0.011
NGC 6171	-0.003	+0.096	+0.090	-0.038	+0.003	+0.028	+0.032	-0.003
NGC 6254	-0.009	+0.079	+0.087	-0.020	-0.009	+0.013	+0.030	-0.000
NGC 6388	+0.032	+0.117	+0.052	-0.071	+0.018	+0.042	+0.018	-0.001
NGC 6397	-0.003	+0.073	+0.081	-0.012	-0.002	+0.007	+0.026	-0.001
NGC 6808	-0.009	+0.078	+0.084	-0.027	-0.011	+0.014	+0.034	-0.002
NGC 6838	+0.005	+0.099	+0.081	-0.042	+0.007	+0.032	+0.029	-0.002
NGC 7078	-0.008	+0.072	+0.078	-0.017	-0.002	+0.006	+0.018	+0.005
NGC 7099	-0.004	+0.073	+0.076	-0.014	-0.002	+0.006	+0.015	+0.003

A.2. Cluster (systematic) errors

In this section we examine the errors that are systematic for all stars in a cluster, but are different for the various clusters considered in this series of paper on the Na-O anticorrelation and HB. Hence, they will have no effect on the star-to-star scatter, but will produce scatter in the relations involving different clusters. We proceed following the same order as considered for the individual star errors.

(i) T_{eff} . As mentioned before, effective temperatures were derived from magnitudes, adopting a mean relation between V or K magnitudes and $T_{\text{eff}}(V-K)$, which in turn are derived from $V-K$ colours using the calibration by Alonso et al. (1999). The $V-K$ colours to be used here are of course the dereddened colours (in the TCS system). Errors in the assumed reddening (and on the zero point of the photometric scales) will cause a systematic shift in the T_{eff} 's.

The reddening estimate we used are from Harris (1996). Assuming an uncertainties of 0.02 mag in $E(B-V)$ this implies

an uncertainty in $E(V-K)$ of $0.02 \times 2.75 = 0.055$ mag. We may then estimate the cluster uncertainty in the T_{eff} 's by multiplying the uncertainty in $E(V-K)$ for the slope of the relation between T_{eff} and $V-K$ derived in each cluster.

Including a (conservative) estimate of 0.02 mag error in the zero point of the $V-K$ colours, and summing this error quadratically to the error in the reddening, the errors come out to be as in column labelled (6) in Table A.2.

(ii) $\log g$. Errors in surface gravity might be obtained by propagating uncertainties in distance modulus (about 0.1 mag), stellar mass (a conservative 10%) and the above systematic errors in effective temperature. The quadratic sum results in errors listed in column (7) of in Table A.2, and is very similar for all clusters.

(iii) v_t . The systematic error in v_t is simply the internal error in v_t divided for the square root of the number of stars (in each

Table A.2. Star-to-star (individual) errors and cluster errors in atmospheric parameters and in the EWs

cluster	star-to-star errors					cluster errors			
	T_{eff}	$\log g$	[A/H]	v_t	EW	T_{eff}	$\log g$	[A/H]	v_t
	(K)	dex	(dex)	(km/s)	(dex)	(K)	dex	(dex)	(km/s)
(1)	(2)	(3)	(4)	(5)	(6)	(7)	(8)	(9)	
NGC 104	6	0.042	0.032	0.11	0.025	40	0.059	0.026	0.009
NGC 288	6	0.041	0.042	0.28	0.025	63	0.061	0.070	0.027
NGC 1904	5	0.041	0.036	0.20	0.027	57	0.060	0.069	0.026
NGC 3201	4	0.041	0.049	0.19	0.028	62	0.061	0.073	0.016
NGC 4590	4	0.041	0.071	0.28	0.037	69	0.061	0.068	0.025
NGC 5904	12	0.041	0.023	0.11	0.024	54	0.060	0.062	0.009
NGC 6121	4	0.041	0.025	0.12	0.022	54	0.060	0.053	0.012
NGC 6171	2	0.041	0.044	0.21	0.025	26	0.057	0.026	0.037
NGC 6254	4	0.041	0.053	0.13	0.026	67	0.061	0.074	0.011
NGC 6388	9	0.043	0.078	0.19	0.037	57	0.061	0.028	0.032
NGC 6397	4	0.041	0.039	0.34	0.038	64	0.060	0.060	0.028
NGC 6808	5	0.041	0.044	0.20	0.027	58	0.060	0.072	0.016
NGC 6838	5	0.041	0.034	0.10	0.023	45	0.059	0.048	0.016
NGC 7078	5	0.041	0.061	0.33	0.030	67	0.061	0.067	0.036
NGC 7099	5	0.041	0.046	0.41	0.034	71	0.061	0.067	0.051

(1) slope relation $T_{\text{eff}}(\text{V-K})_{\text{Alonso}}$ vs mag V or K + 0.02 mag error in V or K

(2) slope $\log g$ vs mag V or K +0.02 mag error + 10% variation in mass

(3) *rms* scatter in [Fe/H] of all analysed stars

(4) quadratic mean of 1σ errors in the slope abundances Fe I/line strength (minus systematic components) from stars with a large enough number of Fe I lines

(5) (*rms* in Fe I for stars with enough lines) divided the square root of typical number of lines

(6) slope relation $T_{\text{eff}}(\text{V-K})_{\text{Alonso}}$ vs $(\text{V-K})_0$ +0.02 error in E(B-V) + 0.02 mag error in V-K colours zero point.

(7) 0.1 mag error in modulus + systematic error in T_{eff} +10% error in mass

(8) statistical error+systematic error in T_{eff} +systematic error in $\log g$ +systematic error in v_t

(9) internal error in v_t divided the square root of N_{stars}

cluster).

(iv) [A/H]. The cluster error we consider here is given by the quadratic sum of four terms: the first 3 are the systematic contribution estimated above multiplied for the appropriate sensitivities in Table A.1. The last one is simply the statistical errors of individual abundance determinations (*rms* scatter divided the square root of the number of stars used in each cluster).

Total systematic errors related to individual clusters are listed in Table A.2.

Table A.3. Error in element ratios due to star-to-star errors in atmospheric parameters and in the EWs

	errors in abundances due to:						total star-to-star error		
	T_{eff}	$\log g$	[A/H]	v_t	<nr>	EW	$T_{\text{eff}}+v_t+\text{EW}$	all	
[Fe/H]I	+0.004	+0.001	+0.003	-0.039	30	0.025	0.046	0.047	NGC 104
[Fe/H]II	-0.006	+0.004	+0.011	-0.017	3	0.078	0.080	0.081	
[O/Fe]	-0.003	+0.003	+0.009	+0.039	1	0.135	0.141	0.141	
[Na/Fe]	+0.001	-0.002	+0.000	+0.010	3	0.078	0.079	0.079	
[Fe/H]I	+0.007	-0.002	-0.002	-0.076	31	0.025	0.080	0.080	NGC 288
[Fe/H]II	-0.003	+0.018	+0.018	-0.034	2	0.098	0.104	0.106	
[O/Fe]	-0.005	+0.018	+0.018	+0.081	1	0.138	0.160	0.162	
[Na/Fe]	-0.002	-0.005	-0.005	+0.050	2	0.098	0.110	0.110	
[Fe/H]I	+0.006	-0.002	-0.004	-0.054	25	0.027	0.061	0.061	NGC 1904
[Fe/H]II	-0.002	+0.017	+0.006	-0.016	2	0.093	0.094	0.096	
[O/Fe]	-0.004	+0.018	+0.014	+0.058	1	0.131	0.143	0.145	
[Na/Fe]	-0.002	-0.005	-0.002	+0.042	3	0.076	0.087	0.087	
[Fe/H]I	+0.005	-0.002	-0.004	-0.042	28	0.028	0.051	0.051	NGC 3201
[Fe/H]II	-0.002	-0.017	+0.010	-0.017	2	0.103	0.104	0.106	
[O/Fe]	-0.004	+0.018	+0.019	+0.046	1	0.146	0.153	0.155	
[Na/Fe]	-0.002	-0.004	-0.000	+0.038	2	0.103	0.110	0.110	
[Fe/H]I	+0.004	-0.001	-0.002	-0.031	12	0.037	0.048	0.048	NGC 4590
[Fe/H]II	-0.001	+0.015	+0.004	-0.014	1	0.129	0.130	0.131	
[O/Fe]	-0.002	+0.016	+0.011	+0.039	1	0.129	0.135	0.136	
[Na/Fe]	-0.002	-0.003	+0.002	+0.025	3	0.074	0.078	0.078	
[Fe/H]I	+0.014	-0.001	-0.002	-0.031	33	0.024	0.042	0.042	NGC 5904
[Fe/H]II	-0.007	+0.018	+0.005	-0.012	2	0.098	0.099	0.101	
[O/Fe]	-0.010	+0.018	+0.009	+0.031	1	0.139	0.143	0.144	
[Na/Fe]	-0.004	-0.006	-0.002	+0.021	3	0.080	0.083	0.083	
[Fe/H]I	+0.004	-0.001	-0.001	-0.037	37	0.022	0.043	0.043	NGC 6121
[Fe/H]II	-0.003	+0.019	+0.006	-0.003	3	0.079	0.079	0.082	
[O/Fe]	-0.003	+0.018	+0.009	+0.008	1	0.136	0.136	0.138	
[Na/Fe]	+0.000	-0.007	-0.003	+0.005	3	0.079	0.079	0.080	
[Fe/H]I	+0.002	-0.001	+0.001	-0.055	37	0.025	0.060	0.060	NGC 6171
[Fe/H]II	-0.001	+0.020	+0.012	-0.027	2	0.109	0.112	0.115	
[O/Fe]	-0.001	+0.018	+0.014	+0.059	1	0.154	0.165	0.166	
[Na/Fe]	+0.000	-0.008	-0.001	+0.032	3	0.089	0.095	0.095	
[Fe/H]I	+0.004	-0.002	-0.005	-0.023	25	0.026	0.035	0.035	NGC 6254
[Fe/H]II	-0.001	+0.016	+0.007	-0.008	2	0.091	0.091	0.093	
[O/Fe]	-0.003	+0.018	+0.016	+0.026	1	0.129	0.132	0.134	
[Na/Fe]	-0.002	-0.004	+0.000	+0.020	3	0.074	0.077	0.077	
[Fe/H]I	+0.003	+0.007	+0.014	-0.084	19	0.037	0.092	0.093	NGC 6388
[Fe/H]II	-0.013	+0.025	+0.033	-0.044	2	0.114	0.123	0.130	
[O/Fe]	-0.001	+0.011	+0.014	+0.086	2	0.114	0.143	0.144	
[Na/Fe]	+0.004	-0.015	-0.001	+0.027	3	0.093	0.097	0.098	
[Fe/H]I	+0.004	-0.001	-0.001	-0.031	16	0.038	0.049	0.049	NGC 6397
[Fe/H]II	-0.001	+0.015	+0.003	-0.010	1	0.153	0.153	0.154	
[O/Fe]	-0.003	+0.017	+0.010	+0.034	1	0.153	0.157	0.158	
[Na/Fe]	-0.002	-0.002	+0.000	+0.031	2	0.108	0.112	0.112	
[Fe/H]I	+0.006	-0.002	-0.005	-0.030	23	0.027	0.041	0.041	NGC 6809
[Fe/H]II	-0.002	+0.016	+0.006	-0.008	2	0.091	0.091	0.093	
[O/Fe]	-0.004	+0.017	+0.015	+0.034	1	0.128	0.132	0.134	
[Na/Fe]	-0.003	-0.006	-0.001	+0.024	2	0.091	0.094	0.094	
[Fe/H]I	+0.005	+0.001	+0.002	-0.032	37	0.023	0.040	0.040	NGC 6838
[Fe/H]II	-0.004	+0.020	+0.011	-0.016	3	0.080	0.082	0.085	
[O/Fe]	-0.005	+0.017	+0.010	+0.033	2	0.098	0.104	0.105	
[Na/Fe]	-0.001	-0.009	-0.001	+0.013	3	0.080	0.081	0.082	
[Fe/H]I	+0.005	-0.002	-0.001	-0.026	13	0.030	0.040	0.040	NGC 7078
[Fe/H]II	-0.001	+0.015	+0.004	-0.007	1	0.111	0.111	0.112	
[O/Fe]	-0.003	+0.016	+0.011	+0.036	1	0.111	0.117	0.118	
[Na/Fe]	-0.002	-0.003	+0.003	+0.023	2	0.078	0.081	0.081	
[Fe/H]I	+0.005	-0.001	-0.001	-0.033	12	0.034	0.048	0.048	NGC 7099
[Fe/H]II	-0.001	+0.015	+0.003	-0.008	1	0.119	0.119	0.120	
[O/Fe]	-0.002	+0.016	+0.007	+0.041	1	0.119	0.126	0.127	
[Na/Fe]	-0.002	-0.003	+0.001	+0.025	2	0.084	0.088	0.088	